

# 14

## Radio-Frequency Linear Accelerators

Resonant linear accelerators are usually single-pass machines. Charged particles traverse each section only once; therefore, the kinetic energy of the beam is limited by the length of the accelerator. Strong accelerating electric fields are desirable to achieve the maximum kinetic energy in the shortest length. Although linear accelerators cannot achieve beam, output energy as high as circular accelerators, the following advantages dictate their use in a variety of applications: (1) the open geometry makes it easier to inject and extract beams; (2) high-flux beams can be transported because of the increased options for beam handling and high-power rf structures; and (3) the duty cycle is high. The duty cycle is defined as the fraction of time that the machine produces beam output.

The operation of resonant linear accelerators is based on electromagnetic oscillations in tuned structures. The structures support a traveling wave component with phase velocity close to the velocity of accelerated particles. The technology for generating the waves and the interactions between waves and particles were described in Chapters 12 and 13. Although the term radio

## Radio-frequency Linear Accelerators

frequency (rf) is usually applied to resonant accelerators, it is somewhat misleading. Although some resonant linear accelerators have been constructed with very large or inductive structures, most present accelerators use resonant cavities or waveguides with dimensions less than 1 m to contain electromagnetic oscillations; they operate in the microwave regime ( $> 300$  MHz).

Linear accelerators are used to generate singly-charged light ion beams in the range of 10 to 300 MeV or multiply charged heavy ions up to 4 GeV (17 MeV/nucleon). These accelerators have direct applications such as radiation therapy, nuclear research, production of short-lived isotopes, meson production, materials testing, nuclear fuel breeding, and defense technology. Ion linear accelerators are often used as injectors to form high-energy input beams for large circular accelerators. The recent development of the radio-frequency quadrupole (RFQ), which is effective for low-energy ions, suggests new applications in the 1-10 MeV range, such as high-energy ion implantation in materials. Linear accelerators for electrons are important tools for high-energy physics research because they circumvent the problems of synchrotron radiation that limit beam energy in circular accelerators. Electron linear accelerators are also used as injectors for circular accelerators and storage rings. Applications for high-energy electrons include the generation of synchrotron radiation for materials research and photon beam generation through the free electron laser process.

Linear accelerators for electrons differ greatly in both physical properties and technological realization from ion accelerators. The contrasts arise partly from dissimilar application requirements and partly from the physical properties of the particles. Ions are invariably non-relativistic; therefore, their velocity changes significantly during acceleration. Resonant linear accelerators for ions are complex machines, often consisting of three or four different types of acceleration units. In contrast, high-gradient electron accelerators for particle physics research have a uniform structure throughout their length. These devices are described in Section 14.1. Electrons are relativistic immediately after injection and have constant velocity through the accelerator. Linear electron accelerators utilize electron capture by strong electric fields of a wave traveling at the velocity of light. Because of the large power dissipation, the machines are operated in a pulsed mode with low-duty cycle. After a description of the general properties of the accelerators, Section 14.1 discusses electron injection, beam breakup instabilities, the design of iris-loaded wave-guides with  $\omega/k = c$ , optimization of power distribution for maximum kinetic energy, and the concept of shunt impedance.

Sections 14.2-14.4 review properties of high-energy linear ion accelerators. The four common configurations of rf ion accelerators are discussed in Sections 14.2 and 14.3: the Wideröe accelerator, the independently-phased cavity array, the drift tube linac, and the coupled cavity array. Starting from the basic Wideröe geometry, the rationale for surrounding acceleration gaps with resonant structures is discussed. The configuration of the drift tube linac is derived qualitatively by considering an evolutionary sequence from the Wideröe device. The principles of coupled cavity oscillations are discussed in Section 14.3. Although a coupled cavity array is more difficult to fabricate than a drift tube linac section, the configuration has a number of benefits for high-flux ion beams when operated in a particular mode (the  $\pi/2$  mode). Coupled cavities have high accelerating gradient, good frequency stability, and strong energy coupling. The latter property is essential for stable electromagnetic oscillations in the presence of significant beam

## Radio-frequency Linear Accelerators

loading. Examples of high-energy ion accelerators are included to illustrate strategies for combining the different types of acceleration units into a high-energy system.

Some factors affecting ion transport in rf linacs are discussed in Section 14.4. Included are the transit-time factor, gap coefficients, and radial defocusing by rf fields. The transit-time factor is important when the time for a particle to cross an acceleration gap is comparable to half the rf period. In this case, the peak energy gain (reflecting the integral of charge times electric field during the transit) is less than the product of charge and peak gap voltage. The transit-time derating factor must be included to determine the synchronous particle orbit. The gap coefficient refers to radial variations of longitudinal electric field. The degree of variation depends on the gap geometry and rf frequency. The spatial dependence of  $E_z$  leads to increased energy spread in the output beam or reduced longitudinal acceptance. Section 14.4 concludes with a discussion of the effects of the radial fields of a slow traveling wave on beam containment. The existence and nature of radial fields are derived by a transformation to the rest frame of the wave in it appears as electrostatic field pattern. The result is that orbits in cylindrically symmetric rf linacs are radially unstable if the particles are in a phase region of longitudinal stability. Ion linacs must therefore incorporate additional focusing elements (such as an FD quadrupole array) to ensure containment of the beam.

Problems of vacuum breakdown in high-gradient rf accelerators are discussed in Section 14.5. The main difference from the discussion of Section 9.5 is the possibility for geometric growth of the number of secondary electrons emitted from metal surfaces when the electron motion is in synchronism with the oscillating electric fields. This process is called multipactoring. Electron multipactoring is sometimes a significant problem in starting up rf cavities; ultimate limits on accelerating gradient in rf accelerators may be set by ion multipactoring.

Section 14.6 describes the RFQ, a recently-developed configuration. The RFQ differs almost completely from other rf linac structures. The fields are azimuthally asymmetric and the main mode of excitation of the resonant structure is a TE mode rather than a TM mode. The RFQ has significant advantages for the acceleration of high-flux ion beams in the difficult low-energy regime (0.1-5 MeV). The structure utilizes purely electrostatic focusing from rf fields to achieve simultaneous average transverse and longitudinal containment. The electrode geometries in the device can be fabricated to generate precise field variations over small-scale lengths. This gives the RFQ the capability to perform beam bunching within the accelerator, eliminating the need for a separate buncher and beam transport system. At first glance, the RFQ appears to be difficult to describe theoretically. In reality, the problem is tractable if we divide it into parts and apply material from previous chapters. The properties of longitudinally uniform RFQs, such as the interdependence of accelerating gradient and transverse acceptance and the design of shaped electrodes, can be derived with little mathematics.

Section 14.7 reviews the racetrack microtron, an accelerator with the ability to produce continuous high-energy electron beams. The racetrack microtron is a hybrid between linear and circular accelerators; it is best classified as a recirculating resonant linear accelerator. The machine consists of a short linac (with a traveling wave component with  $\omega/k = c$ ) and two regions of uniform magnetic field. The magnetic fields direct electrons back to the entrance of the accelerator in synchronism with the rf oscillations. Energy groups of electrons follow separate

## Radio-frequency Linear Accelerators

orbits which require individual focusing and orbit correction elements. Synchrotron radiation limits the beam kinetic energy of microtrons to less than 1 GeV. Beam breakup instabilities are a major problem in microtrons; therefore, the output beam current is low ( $< 100 \mu\text{A}$ ). Nonetheless, the high-duty cycle of microtrons means that the time-averaged electron flux is much greater than that from conventional electron linacs.

### 14.1 ELECTRON LINEAR ACCELERATORS

Radio-frequency linear accelerators are used to generate high-energy electron beams in the range of 2 to 20 GeV. Circular electron accelerators cannot reach high output kinetic energy because of the limits imposed by synchrotron radiation. Linear accelerators for electrons are quite different from ion accelerators. They are high-gradient, traveling wave structures used primarily for particle physics research. Accelerating gradient is the main figure of merit; consequently, the efficiency and duty cycle of electron linacs are low. Other accelerator configurations are used when a high time-averaged flux of electrons at moderate energy is required. One alternative, the racetrack microtron, is described in Section 14.7.

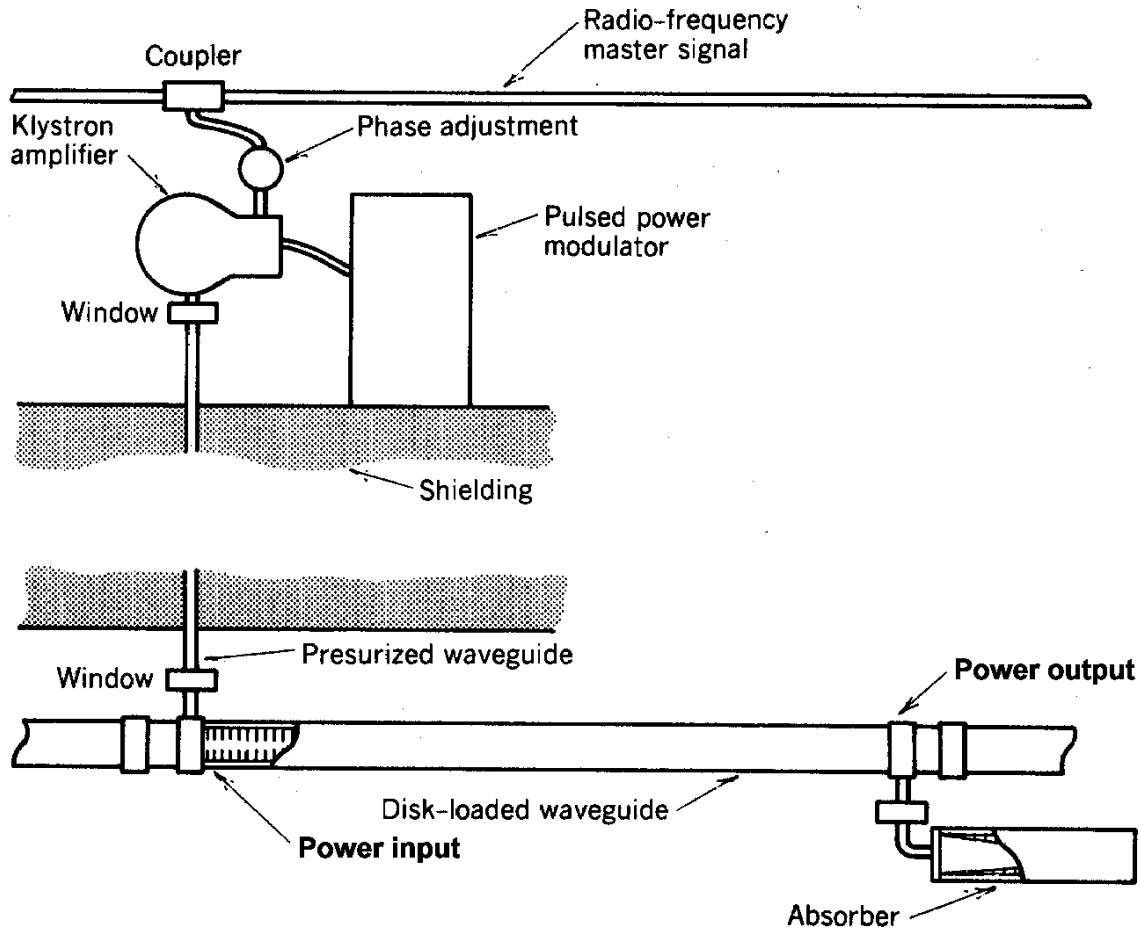
#### A. General Properties

Figure 14.1 shows a block diagram of an electron linac. The accelerator typically consists of a sequence of identical, iris-loaded slow-wave structures that support traveling waves. The waveguides are driven by high-power klystron microwave amplifiers. The axial electric fields of the waves are high, typically on the order of 8 MV/m. Parameters of the 20-GeV accelerator at the Stanford Linear Accelerator Center are listed in Table 14.1. The accelerator is over 3 km in length; the open aperture for beam transport is only 2 cm in diameter. The successful transport of the beam through such a long, narrow tube is a consequence of the relativistic contraction of the apparent length of the accelerator (Section 13.6). A cross section of the accelerator is illustrated in Figure 14.2. A scale drawing of the rf power distribution system is shown in Figure 14.3.

The features of high-energy electron linear accelerators are determined by the following considerations.

1. Two factors motivate the use of strong accelerating electric fields: (a) high gradient is favorable for electron capture (Section 13.6) and (b) the accelerator length for a given final beam energy is minimized.
2. Resistive losses per unit length are large in a high-gradient accelerator because power dissipation in the waveguide walls scales as  $E_z^2$ . Dissipation is typically greater than 1 MW/m. Electron linacs must be operated on an intermittent duty cycle with a beam pulselength of a few microseconds.

## Radio-frequency Linear Accelerators



**Figure 14.1** High-energy linear electron accelerator.

3. An iris-loaded waveguide with relatively large aperture can support slow waves with  $\omega/k = c$ . Conduction of rf energy along the waveguide is effective; nonetheless, the waves are attenuated because of the high losses. There is little to be gained by reflecting the traveling waves to produce a standing wave pattern. In practice, the energy of the attenuated wave is extracted from the waveguide at the end of an accelerating section and deposited in an external load. This reduces heating of the waveguides.

4. A pulsed electron beam is injected after the waveguides are filled with rf energy. The beam pulse length is limited by the accelerator duty cycle and by the growth of beam breakup instabilities. Relatively high currents ( $\leq 0.1$  A) are injected to maximize the number of electrons available for experiments.

## Radio-frequency Linear Accelerators

**TABLE 14.1 Parameters of the Stanford Linear Accelerator**

Accelerator length	3100 m
Length between power feeds	3.1 m
Number of accelerator sections	960
Number of klystrons	245
Peak power per klystron	6–24 MW
Beam pulse repetition rate	1–360 pulses/s
Radio-frequency pulse length	2.5 $\mu$ s
Filling time	0.83 $\mu$ s
Shunt impedance	53 M $\Omega$ /m
Electron energy (unloaded)	11.1–22.2 GeV
Electron energy (loaded)	10–20 GeV
Electron beam peak current	25–50 mA
Electron beam average current	15–30 $\mu$ A
Average electron beam power	0.15–0.6 MW
Efficiency	4.3%
Positron energy	7.4–14.8 GeV
Positron average beam current	0.45 $\mu$ A
Operating frequency	2.856 GHz
Accelerating structure	Iris-loaded waveguide
Waveguide outer diameter	10.5 cm
Aperture diameter	1.9 cm

5. The feasibility of electron linacs is a consequence of technological advances in high-power rf amplifiers. Klystrons can generate short pulses of rf power in the 30-MW range with good frequency stability. High-power klystrons are driven by pulsed power modulators such as the PFN discussed in Section 9.12.

The waveguides of the 2.5-GeV accelerator at the National Laboratory for High Energy Physics (KEK), Tsukuba, Japan, have a diameter of 0.1 m and an operating frequency of 2.856 GHz. The choice of frequency results from the availability of high-power klystrons from the development of the SLAC accelerator. An acceleration unit consists of a high-power coupler, a series of four iris-loaded waveguides, a decoupler, and a load. The individual wave-guides are 2 m long. The inner radius of the irises has a linear taper of 75  $\mu$ m per cell along the length of the guide; this maintains an approximately constant  $E_z$  along the structure, even though the traveling wave is

## Radio-frequency Linear Accelerators

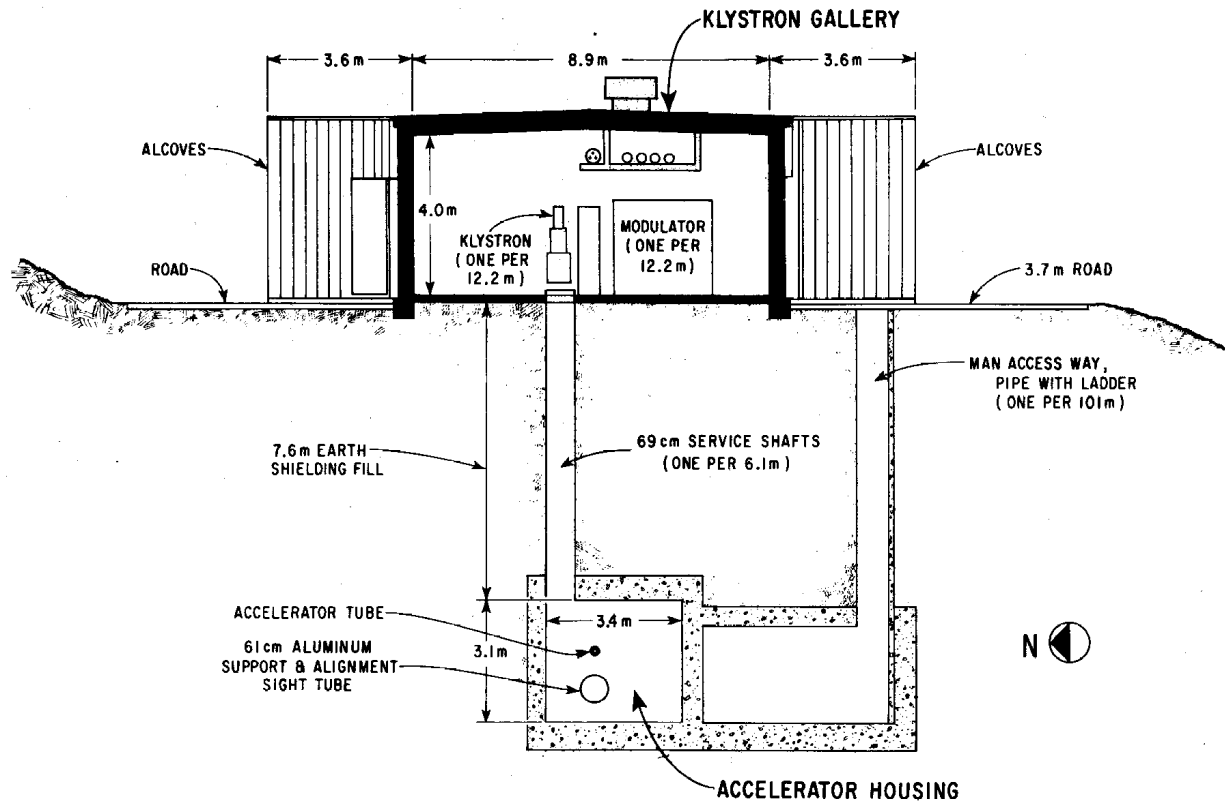


**Figure 14.2** Stanford Linear Accelerator; cross section. (Courtesy W. B. Herrmannsfeldt, Stanford Linear Accelerator Center.)

## Radio-frequency Linear Accelerators

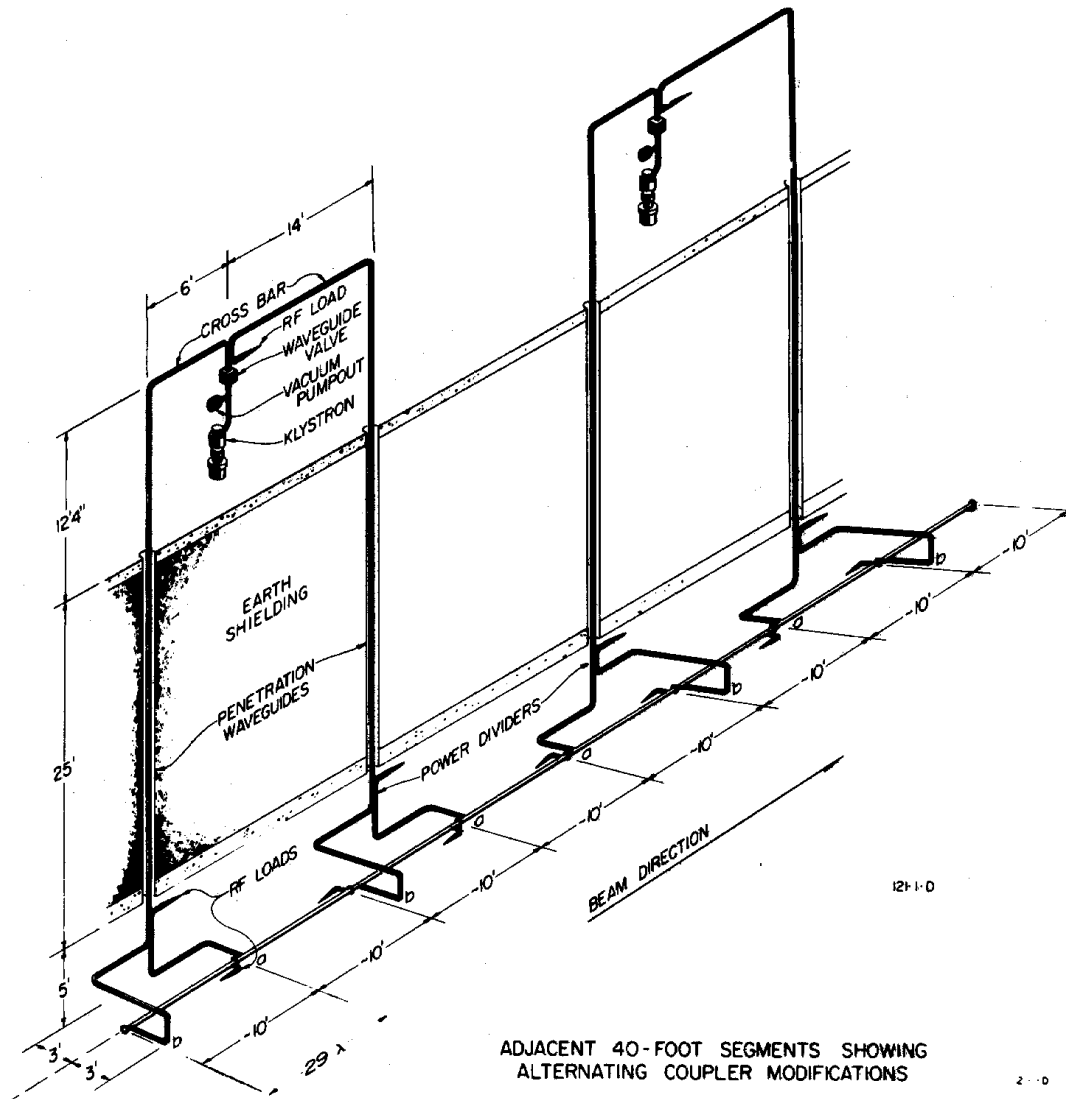


**Figure 14.3** Stanford Linear Accelerator; arrangement of rf power system. (Courtesy W. B. Herrmannsfeldt, Stanford Linear Accelerator Center.)

attenuated. Individual waveguides of a unit have the same phase velocity but vary in the relative dimensions of the wall and iris to compensate for their differing distance from the rf power input. There are five types of guides in the accelerator; the unit structure is varied to minimize propagation of beam-excited modes which could contribute to the beam breakup instability. Construction of the guides utilized modern methods of electroplating and precision machining. A dimensional accuracy of  $\pm 2 \mu\text{m}$  and a surface roughness of  $200 \text{ \AA}$  was achieved, making postfabrication tuning unnecessary.

### B. Injection

The pulsed electron injector of a high-power electron linear accelerator is designed for high voltage ( $> 200$  kV) to help in electron capture. The beam pulselength may vary from a few nanoseconds to  $1 \mu\text{s}$  depending on the research application. The high-current beam must be aimed with a precision of a few milliradians to prevent beam excitation of undesired rf modes in the accelerator. Before entering the accelerator, the beam is compressed into micropulses by a buncher. A buncher consists of an rf cavity or a short section of iris-loaded waveguide operating at the same frequency as the main accelerator. Electrons emerge from the buncher cavity with a longitudinal velocity dispersion. Fast particles overtake slow particles, resulting in downstream localization of the beam current to sharp spikes. The electrons must be confined within a small spread in phase angle ( $\leq 5^\circ$ ) to minimize the kinetic energy spread of the output beam.

The micropulses enter the accelerator at a phase between  $0^\circ$  and  $90^\circ$ . As we saw in Section 13.6, the average phase of the pulse increases until the electrons are ultra-relativistic. For the remainder of the acceleration cycle, acceleration takes place near a constant phase called the *asymptotic phase*. The injection phase of the micropulses and the accelerating gradient are adjusted to give an asymptotic phase of  $90^\circ$ . This choice gives the highest acceleration gradient and the smallest energy spread in the bunch.

Output beam energy uniformity is a concern for high-energy physics experiments. The output energy spread is affected by variations in the traveling wave phase velocity. Dimensional tolerances in the waveguides on the order of  $10^{-3}$  cm must be maintained for a 1% energy spread. The structures must be carefully machined and tuned. The temperature of the waveguides under rf power loading must be precisely controlled to prevent a shift in phase velocity from thermal expansion.

### C. Beam Breakup Instability

The theory of Section 13.6 indicated that transverse focusing is unnecessary in an electron linac because of the shortened effective length. This is true only at low beam current; at high current, electrons are subject to the *beam breakup instability* [W. K. H. Panofsky and M. Bander, Rev. Sci. Instrum. **39**, 206 (1968); V. K. Neil and R. K. Cooper, Part. Accel. **1**, 111 (1970)] also known as the *transverse instability* or *pulse shortening*. The instability arises from excitation of  $\text{TM}_{110}$  cavity modes in the spaces between irises. Features of the  $\text{TM}_{110}$  mode in a cylindrical cavity are illustrated in Figure 14.4. Note that there are longitudinal electric fields of opposite polarity in the upper and lower portions of the cavity and that there is a transverse magnetic field on the axis. An electron micropulse (of sub-nanosecond duration) can be resolved into a broad spectrum of frequencies. If the pulse has relatively high current and is eccentric with respect to the cavity, interaction between the electrons and the longitudinal electric field of the  $\text{TM}_{110}$  mode

## Radio-frequency Linear Accelerators

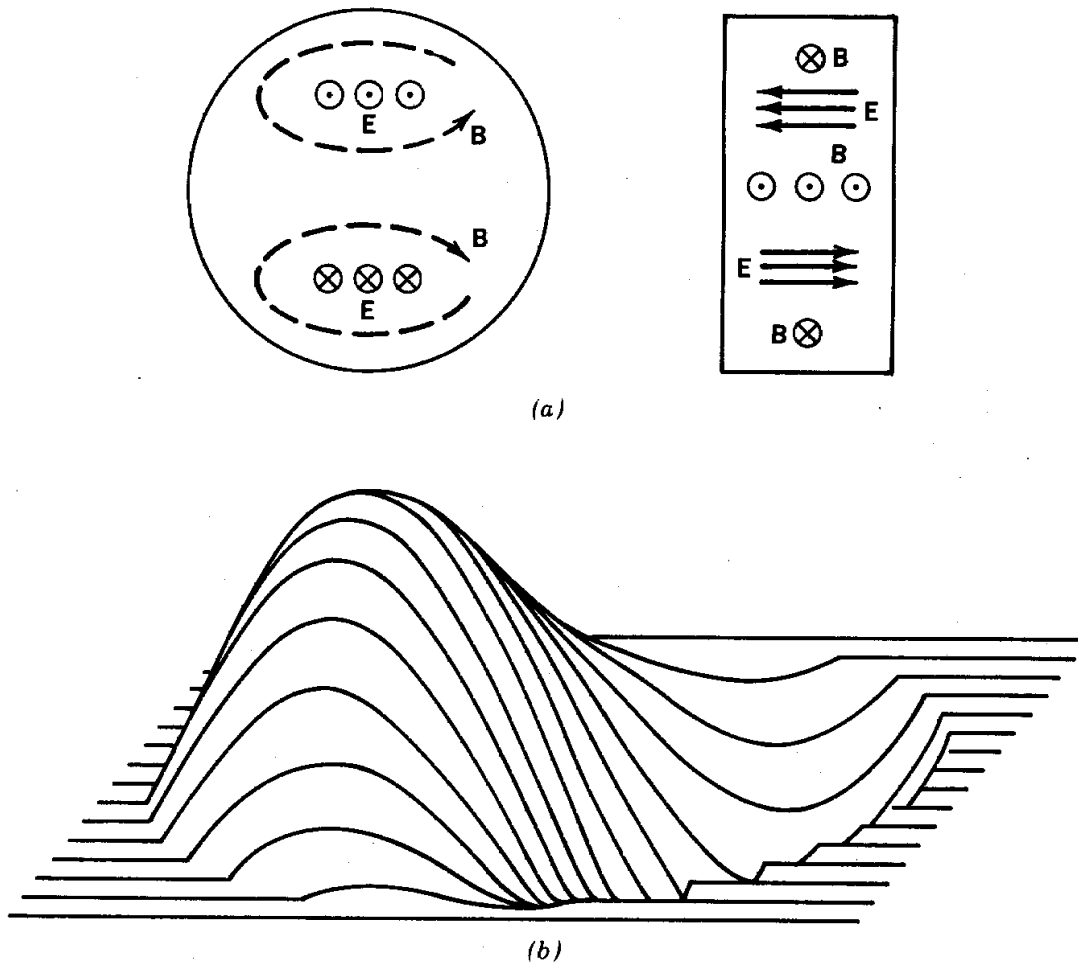


**Figure 14.4**  $TM_{110}$  mode in cylindrical cavity. (a) diagram of electric and magnetic field distributions. (b) Three-dimensional plot of peak electric field amplitude as function of position.

takes place. The mode is excited near the entrance of the accelerator by the initial micropulses of the macropulse. The magnetic field of the mode deflects subsequent portions of the macropulse, causing transverse sweeping of the beam at frequency  $\omega_{110}$ . The sweeping beam can transfer energy continually to  $TM_{110}$  excitations in downstream cavities. The result is that beam sweeping grows from the head to the tail of the microsecond duration macropulse and the strength of  $TM_{110}$  oscillations grows along the length of the machine. Sweeping motion leads to beam loss. The situation is worsened if the  $TM_{110}$  excitation can propagate backward along the iris-loaded waveguide toward the entrance to the accelerator or if the beam makes many passes through the same section of accelerator (as in the microtron). This case is referred to as the *regenerative beam breakup instability*.

## Radio-frequency Linear Accelerators

The beam breakup instability has the following features.

1. Growth of the instability is reduced by accurate injection of azimuthally symmetric beams.
2. The energy available to excite undesired modes is proportional to the beam current. Instabilities are not observed below a certain current; the cutoff depends on the macropulse length and the Q values of the resonant structure.
3. The amplitude of undesired modes grows with distance along the accelerator and with time. This explains pulse shortening, the loss of late portions of the electron macropulse.
4. Mode growth is reduced by varying the accelerator structure. The phase velocity for  $TM_{01}$  traveling waves is maintained constant, but the resonant frequency for  $TM_{110}$  standing waves between irises is changed periodically along the accelerator.

Transverse focusing elements are necessary in high-energy electron linear accelerators to counteract the transverse energy gained through instabilities. Focusing is performed by solenoid lenses around the waveguides or by magnetic quadrupole lenses between guide sections.

### D. Frequency Equation

The dispersion relationship for traveling waves in an iris-loaded waveguide was introduced in Section 12-10. We shall determine the approximate relationship between the inner and outer radii of the irises for waves with phase velocity  $\omega/k = c$  at a specified frequency. The *frequency equation* is a first-order guide. A second-order waveguide design is performed with computer calculations and modeling experiments.

Assume that  $\delta$ , the spacing between irises, is small compared to the wavelength of the traveling wave; the boundary fields approximate a continuous function. The tube radius is  $R_o$  and the aperture radius is  $R$ . The complete solution consists of standing waves in the volume between the irises and a traveling wave matched to the reactive boundary at  $r = R_o$ . The solution must satisfy the following boundary conditions:

$$E_z(\text{standing wave}) = 0 \quad \text{at } r = R_o, \quad (14.1)$$

$$E_z(\text{traveling wave}) \cong E_z(\text{standing wave}) \quad \text{at } r = R, \quad (14.2)$$

$$B_\theta(\text{traveling wave}) \cong B_\theta(\text{standing wave}) \quad \text{at } r = R. \quad (14.3)$$

The last two conditions proceed from the fact that  $\mathbf{E}$  and  $\mathbf{B}$  must be continuous in the absence of surface charges or currents.

## Radio-frequency Linear Accelerators

Following Section 12.3, the solution for azimuthally symmetric standing waves in the space between the irises is

$$E_z(r,t) = A J_0(\omega r/c) + B Y_0(\omega r/c). \quad (14.4)$$

The  $Y_0$  term is retained because the region does not include the axis. Applying Eq. (14.1), Eq. (14.4) becomes

$$E_z = E_o [Y_0(\omega R_o/c) J_0(\omega r/c) - J_0(\omega R_o/c) Y_0(\omega r/c)]. \quad (14.5)$$

The toroidal magnetic field is determined from Eq. (12.45) as

$$B_\theta = - (jE_o/c) [Y_0(\omega R_o/c) J_1(\omega r/c) - J_0(\omega R_o/c) Y_1(\omega r/c)]. \quad (14.6)$$

The traveling wave has an electric field of the form  $E_z = E_o \exp[j(kz - \omega t)]$ . We shall see in Section 14.4 that the axial electric field of the traveling wave is approximately constant over the aperture. Therefore, the net displacement current carried by a wave with phase velocity equal to  $c$  is

$$I_d = \pi R^2 (\partial E_z / \partial t) / \mu_o c^2 = - (j\omega / \mu_o c^2) (\pi R^2) E_o \exp[j(kz - \omega t)]. \quad (14.7)$$

The toroidal magnetic field of the wave at  $r = R$  is

$$B_\theta = - (j\omega R / 2c^2) E_o \exp[j(kz - \omega t)]. \quad (14.8)$$

The frequency equation is determined by setting  $E_z/B_\theta$  for the cavities and for the traveling wave equal at  $r = R$  [Eqs. (14.2) and (14.3)]:

$$\omega R/c = \frac{2 [Y_0(\omega R_o/c) J_1(\omega R/c) - J_0(\omega R_o/c) Y_1(\omega R/c)]}{Y_0(\omega R_o/c) J_0(\omega R/c) - J_0(\omega R_o/c) Y_0(\omega R/c)}. \quad (14.9)$$

Equation (14.9) is a transcendental equation that determines  $\omega$  in terms of  $R$  and  $R_o$  to generate a traveling wave with phase velocity equal to the speed of light. A plot of the right-hand side of the equation is given in Figure 14.5. A detailed analysis shows that power flow is maximized and losses minimized when there are about four irises per wavelength. Although the assumptions underlying Eq. (14.9) are not well satisfied in this limit, it still provides a good first-order estimate.

## Radio-frequency Linear Accelerators

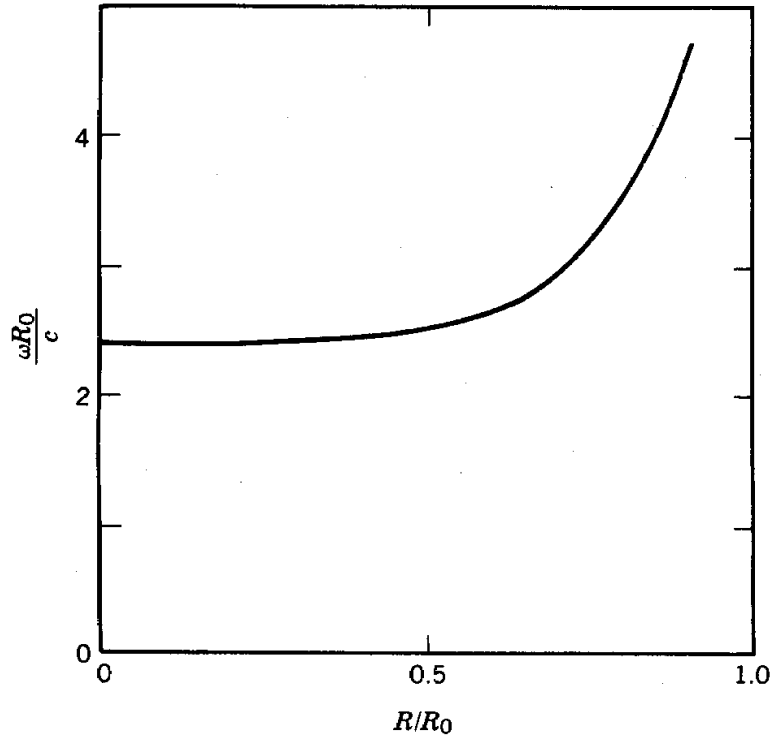


**Figure 14.5** Frequency of  $TM_{01}$  mode with  $\omega/k = c$  in iris-loaded cylindrical waveguide as function of  $R/R_0$ , where  $R$  is iris inner radius and  $R_0$  is inner radius of waveguide.

### E. Electromagnetic Energy Flow

Radio-frequency power is inserted into the waveguides periodically at locations separated by a distance  $l$ . For a given available total power  $P$ , and accelerator length  $L$ , we can show that there is an optimum value of  $l$  such that the final beam energy is maximized. In analogy with standing wave cavities, the quantity  $Q$  characterizes resistive energy loss in the waveguide according to

$$-(dP/dz) = U\omega/Q. \quad (14.10)$$

In Eq. (14.10),  $dP/dz$  is the power lost per unit length along the slow-wave structure and  $U$  is the electromagnetic energy per unit length. Following the discussion of Section 12.10, the group velocity of the traveling waves is equal to

$$v_g = \frac{\text{energy flux}}{\text{electromagnetic energy density}}.$$

Multiplying the numerator and denominator by the area of the waveguide implies

## Radio-frequency Linear Accelerators

$$Uv_g = P, \quad (14.11)$$

where  $P$  is the total power flow. Combining Eqs. (14.10) and (14.11),  $-(dP/dz) = (\omega/Qv_g) P$ , or

$$P(z) = P_o \exp(-\omega z/Qv_g), \quad (14.12)$$

where  $P_o$  is the power input to a waveguide section at  $z = 0$ . The electromagnetic power flow is proportional to the Poynting vector  $\mathbf{S} = \mathbf{E} \times \mathbf{H} \sim E_z^2$  where  $E_z$  is the magnitude of the peak axial electric field. We conclude that electric field as a function of distance from the power input is described by

$$E_z(z) = E_{zo} \exp(-z/l_o), \quad (14.13)$$

where  $l_o = 2Qv_g/\omega$ . An electron traveling through an accelerating section of length  $l$  gains an energy

$$\Delta T = e \int_0^l E_z(z) dz. \quad (14.14)$$

Substituting from Eq. (14.13) gives

$$\Delta T = eE_{zo}l [1 - \exp(-l/l_o)] / (l/l_o). \quad (14.15)$$

In order to find an optimum value of  $l$ , we must define the following constraints:

1. The total rf power  $P_t$  and total accelerator length  $L$  are specified. The power input to an accelerating section of length  $l$  is  $\Delta P = P_t (l/L)$ .

2. The waveguide properties  $Q$ ,  $v_g$ , and  $\omega$  are specified.

The goal is to maximize the total energy  $T = \Delta T (L/l)$  by varying the number of power input points. The total power scales as

$$P_t \sim (v_g E_{zo}^2) (L/l),$$

where the first factor is proportional to the input power flux to a section and the second factor is the number of sections. Therefore, with constant power,  $E_{zo}$  scales as  $\sqrt{l}$ . Substituting the scaling for  $E_{zo}$  in Eq. (14.15) and multiplying by  $L/l$ , we find that the beam output energy scales as

## Radio-frequency Linear Accelerators

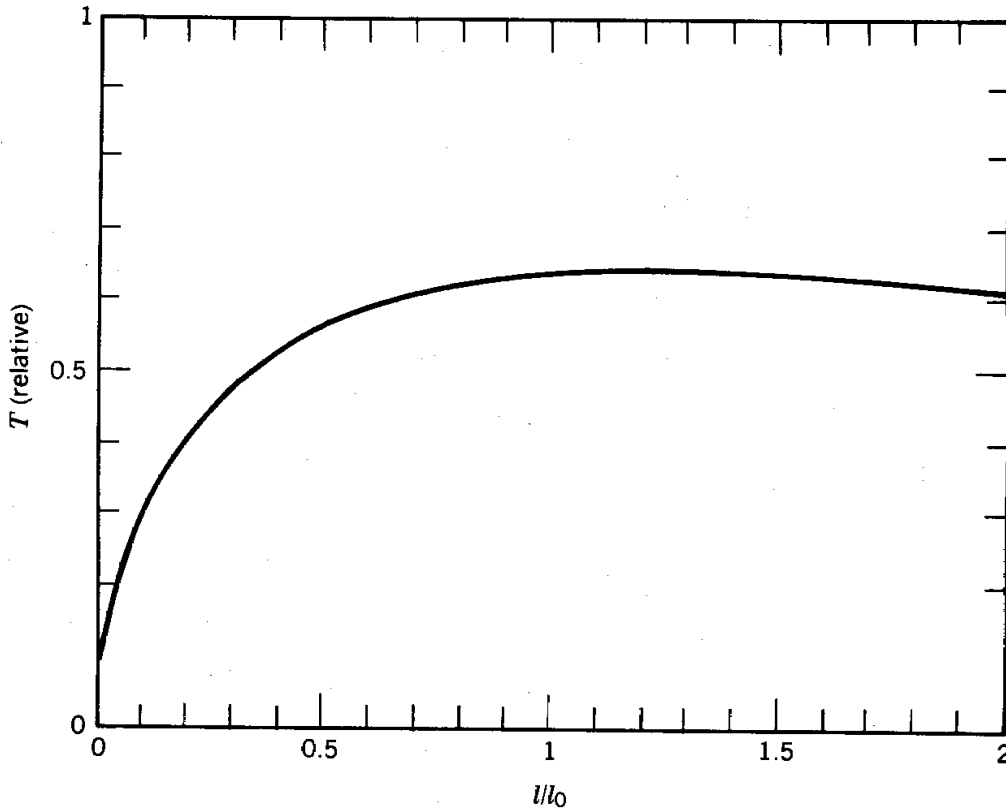


**Figure 14.6** Relative output beam kinetic energy from traveling wave electron accelerator as function of  $l/l_0$ , where  $l_0 = 2Qv_g/\omega$ :  $Q$  is quality factor of waveguide,  $v_g$  is group velocity of traveling waves in slow-wave structure, and  $\omega$  is rf angular frequency).

$$T \sim \sqrt{l} [1 - \exp(-l/l_0)]/l$$

or

$$T \sim [1 - \exp(-l/l_0)] / \sqrt{l/l_0}. \quad (14.16)$$

Inspection of Figure 14.6 shows that  $T$  is maximized when  $l/l_0 = 1.3$ ; the axial electric field drops to 28% of its initial value over the length of a section. It is preferable from the point of view of particle dynamics to maintain a constant gradient along the accelerator. Figure 14.6 implies that  $l/l_0$  can be reduced to 0.8 with only a 2% drop in the final energy. In this case, the output electric field in a section is 45% of the initial field.

Fields can also be equalized by varying waveguide properties over the length of a section. If the

## Radio-frequency Linear Accelerators

wall radius and the aperture radius are decreased consistent with Eq. (14.9), the phase velocity is maintained at  $c$  while the axial electric field is raised for a given power flux. Waveguides can be designed for constant axial field in the presence of decreasing power flux. In practice, it is difficult to fabricate precision waveguides with continuously varying geometry. A common compromise is to divide an accelerator section into subsections with varying geometry. The sections must be carefully matched so that there is no phase discontinuity between them. This configuration has the additional benefit of reducing the growth of beam breakup instabilities.

### F. Shunt Impedance

The *shunt impedance* is a figure-of-merit quantity for electron and ion linear accelerators. It is defined by

$$P_t = V_o^2 / (Z_s L), \quad (14.17)$$

where  $P_t$  is the total power dissipated in the cavity walls of the accelerator,  $V_o$  is the total accelerator voltage (the beam energy in electron volts divided by the particle charge), and  $L$  is the total accelerator length. The shunt impedance  $Z_s$  has dimensions of ohms per meter. An alternate form for shunt impedance is

$$Z_s = \overline{E_z^2} / (dP/dz), \quad (14.18)$$

where  $dP/dz$  is the resistive power loss per meter. The power loss of Eq. (14.17) has the form of a resistor of value  $Z_s L$  in parallel with the beam load. This is the origin of the term shunt impedance.

The efficiency of a linear accelerator is given by

$$\text{energy efficiency} = Z_b / (Z_b + Z_s L), \quad (14.19)$$

where  $Z_b$  is the beam impedance,  $Z_b = V_o / i_b$ . The shunt impedance for most accelerator rf structures lies in the range of 25 to 50 M $\Omega$ /m. As an example, consider a 2.5-GeV linear electron accelerator with a peak on-axis gradient of 8 MV/m. The total accelerator length is 312 m. With a shunt impedance of 50 M $\Omega$ /m, the total parallel resistance is  $1.6 \times 10^{10}$   $\Omega$ . Equation (14.17) implies that the power to maintain the high acceleration gradient is 400 MW.

## 14.2 LINEAR ION ACCELERATOR CONFIGURATIONS

Linear accelerators for ions differ greatly from electron machines. Ion accelerators must support

## Radio-frequency Linear Accelerators

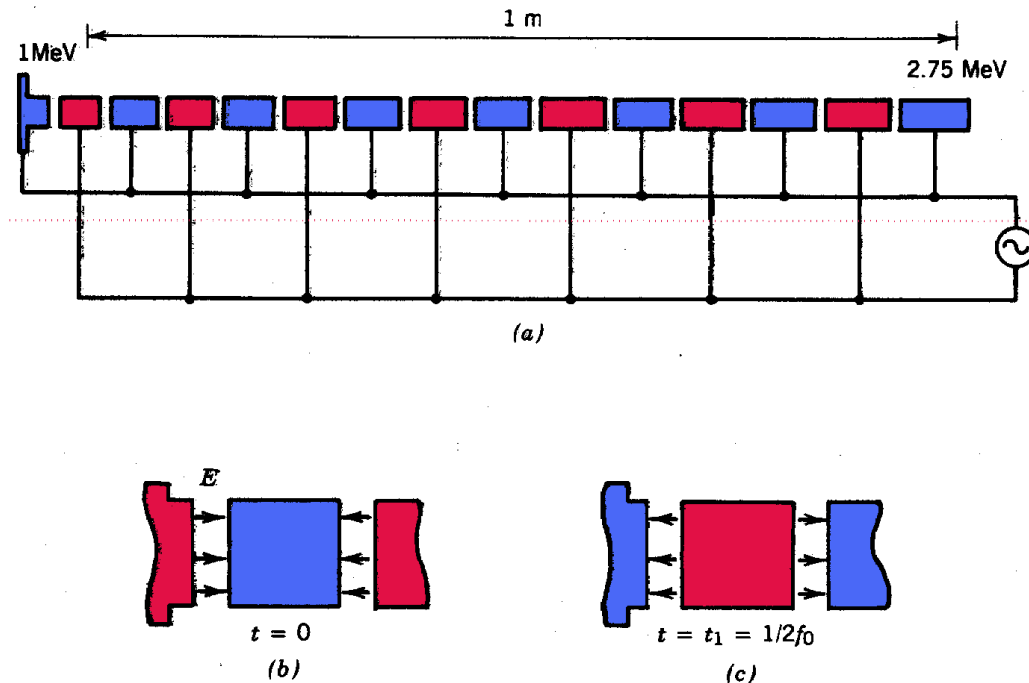


**Figure 14.7** Wideröe linear accelerator for heavy ions. (a) Scale drawing of accelerator with following parameters: Ion species: Cs-137,  $f = 10$  MHz,  $T_i = 1$  MeV,  $V_0 = 100$  kV, and  $\phi_s = 60^\circ$ . (b) Electric fields in acceleration gaps 1 and 2 at ion injection ( $t = 0$ ). (c) Electric fields at time  $t = 1/2f$ , where  $f$  is the rf frequency.

traveling wave components with phase velocity well below the speed of light. In the energy range accessible to linear accelerators, ions are non-relativistic; therefore, there is a considerable change in the synchronous particle velocity during acceleration. Slow-wave structures are not useful for ion acceleration. An iris-loaded waveguide has small apertures for  $\omega/k \ll c$ . The conduction of electromagnetic energy via slow waves is too small to drive a multi-cavity waveguide. Alternative methods of energy coupling are used to generate traveling wave components with slow phase velocity.

An ion linear accelerator typically consists of a sequence of cylindrical cavities supporting standing waves. Cavity oscillations are supported either by individual power feeds or through inter-cavity coupling via magnetic fields. The theory of ion accelerators is most effectively carried out by treating cavities as individual oscillators interacting through small coupling terms.

Before studying rf linear ion accelerators based on microwave technology, we will consider the Wideröe accelerators [R. Wideroe, Arch. Elektrotechn. **21**, 387 (1928)] (Fig. 14.7a), the first successful linear accelerator. The Wideröe accelerator operates at a low frequency (1-10 MHz); it still has application for initial acceleration of heavy ions. The device consists of a number of tubes concentric with the axis connected to a high-voltage oscillator. At a particular time, half the tubes are at negative potential with respect to ground and half the tubes are positive. Electric fields are concentrated in narrow acceleration gaps; they are excluded from the interior of the

## Radio-frequency Linear Accelerators

tubes. The tubes are referred to as *drift tubes* because ions drift at constant velocity inside the shielded volume. Assume that the synchronous ion crosses the first gap at  $t = 0$  when the fields are aligned as shown in Figure 14.7b. The ion is accelerated across the gap and enters the zero-field region in the first drift tube. The ion reaches the second gap at time

$$\Delta t_1 = L_1/v_{s1}. \quad (14.20)$$

The axial electric fields at  $t = t_1$  are distributed as shown in Figure 14.7c if  $t_1$  is equal to half the rf period, or

$$\Delta t_1 = \pi/\omega. \quad (14.21)$$

The particle is accelerated in the second gap when Eq. (14.21) holds.

It is possible to define a synchronous orbit with continuous acceleration by increasing the length of subsequent drift tubes. The velocity of synchronous ions following the  $n$ th gap is

$$V_1 (LC_c \omega_o^2) + V_2 (1 - LC\omega^2 - LC_c \omega_o^2) = 0. \quad (14.22)$$

here  $T_o$  is the injection kinetic energy,  $V_o$  is the peak gap voltage, and  $\phi_s$  is the synchronous phase. The length of drift tube  $n$  is

$$L_n = v_n (\pi/\omega). \quad (14.23)$$

The drift tubes of Figure 14.7a are drawn to scale for the acceleration of  $Hg^+$  ions injected at 2 MeV with a peak gap voltage of 100 kV and a frequency of 4 MHz.

The Wideröe accelerator is not useful for light-ion acceleration and cannot be extrapolated to produce high-energy heavy ions. At high energy, the drift tubes are unacceptably long, resulting in a low average accelerating gradient. The drift tube length is reduced if the rf frequency is increased, but this leads to the following problems:

1. The acceleration gaps conduct large displacement currents at high frequency, loading the rf generator.
2. Adjacent drift tubes act as dipole antennae at high frequency with attendant loss of rf energy by radiation.

The high-frequency problems are solved if the acceleration gap is enclosed in a cavity with resonant frequency  $\omega$ . The cavity walls reflect the radiation to produce a standing electromagnetic oscillation. The cavity inductance in combination with the cavity and gap capacitance constitute an  $LC$  circuit. Displacement currents are supported by the electromagnetic oscillations. The power supply need only contribute energy to compensate for resistive losses and beam loading.

## Radio-frequency Linear Accelerators

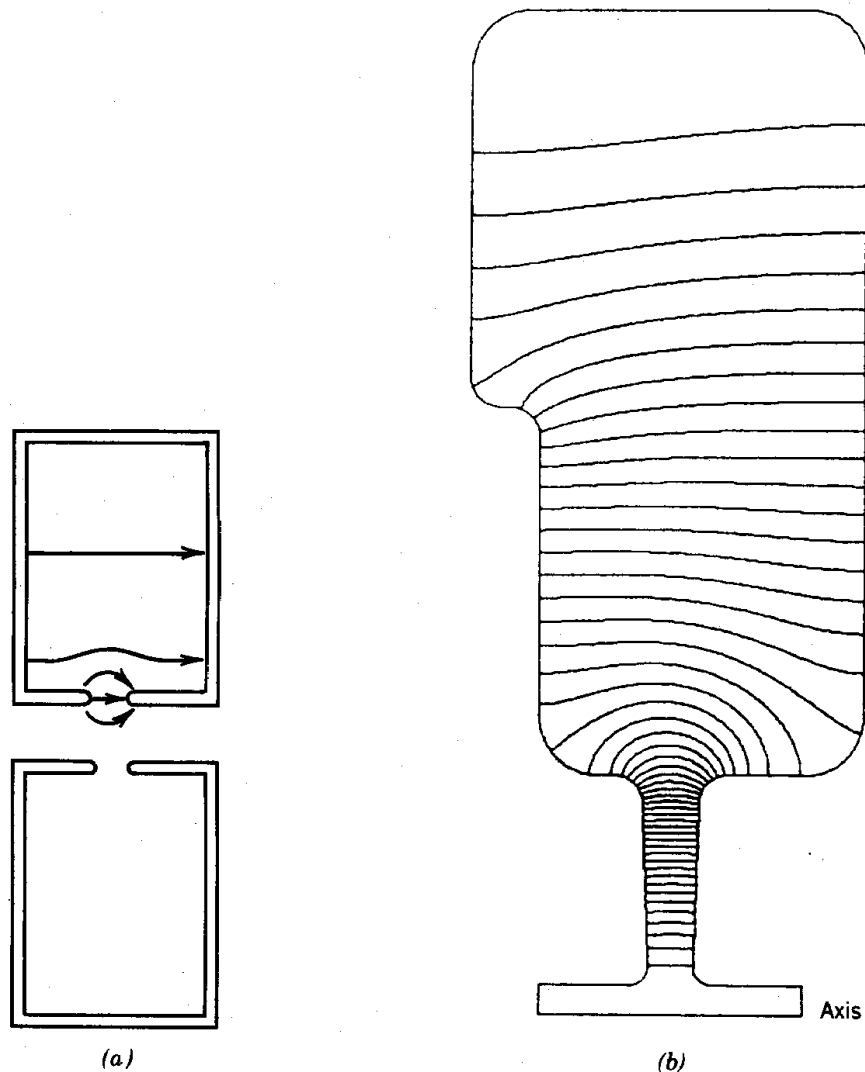


**Figure 14.8** Resonant cavities for particle acceleration. (a) Electric fields in cylindrical cavity with “noses” to define beam drift space. (b) Computer calculation of electric fields of an acceleration cavity using the SUPERFISH code;  $f = 454$  MHz. (Courtesy G. Boicourt, Los Alamos National Laboratory.)

A resonant cavity for ion acceleration is shown in Figure 14.8a. The  $TM_{010}$  mode produces good electric fields for acceleration. We have studied the simple cylindrical cavity in Section 12.3. The addition of drift tube extensions to the cylindrical cavity increases the capacitance on axis, thereby lowering the resonant frequency. The resonant frequency can be determined by a perturbation analysis or through the use of computer codes. The electric field distribution for a linac cavity computed by the program SUPERFISH is shown in Figure 14.8b.

Linear ion accelerators are composed of an array of resonant cavities. We discussed the synthesis of slow waves by independently phased cavities in Section 12.9. Two frequently

## Radio-frequency Linear Accelerators

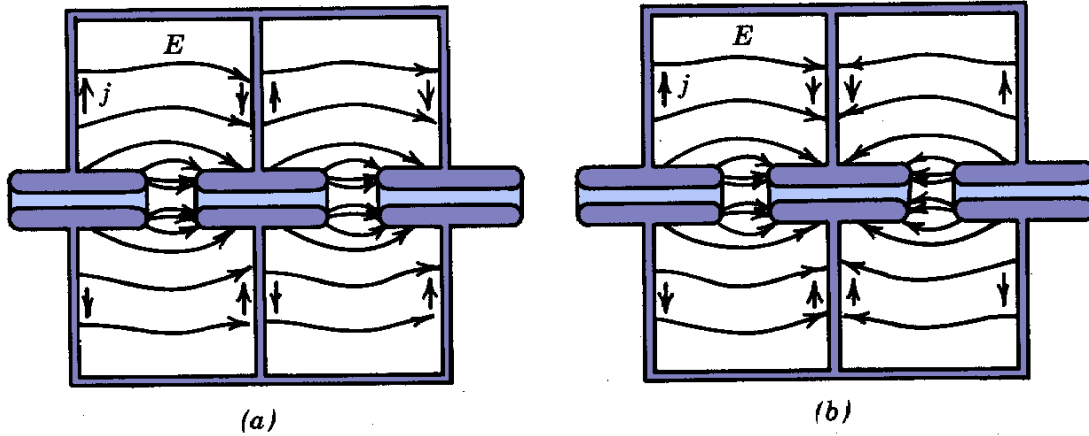


**Figure 14.9** Electric field lines and wall currents of  $TM_{010}$  modes in two cavities of standing wave linear accelerator: (a)  $\beta\lambda$  linac, (b)  $\frac{1}{2}\beta\lambda$  linac.

encountered cases of cavity phasing are illustrated in Figures 14.9a and 14.9b. In the first, the electric fields of all cavities are in phase, while in the second there is a phase change of  $180^\circ$  between adjacent cavities. The synchronous condition for the in-phase array is satisfied if ions traverse the inter-gap distance  $L_n$  in one rf period:

$$L_n = v_n (2\pi/\omega) = \beta\lambda, \quad (14.24)$$

where  $\beta = v_n/c$  and  $\lambda = 2\pi c/\omega$ . Hence, an accelerator with the phasing of Figure 14.9a is referred to as a  $\beta\lambda$  linac. Similarly, the accelerator of Figure 14.9b is a  $\beta\lambda/2$  linac because the synchronous condition implies that

$$L_n = \beta\lambda/2. \quad (14.25)$$

In this notation, the Wideröe accelerator is a  $\beta\lambda/2$  structure.

The advantages of an individually-phased array are that all cavities are identical and that a uniform accelerating gradient can be maintained. The disadvantage is technological; each cavity requires a separate rf amplifier and waveguide. The cost of the accelerator is reduced if a number of cavities are driven by a single power supply at a single feed point. Two geometries that accomplish this are the *drift tube* or *Alvarez linac* [L.W. Alvarez, Phys. Rev. **70**, 799 (1946)] and the *coupled cavity array*. We shall study the drift tube accelerator in the remainder of this section. Coupled cavities are treated in Section 14.3.

The concept of the drift tube linac is most easily understood by following an evolution from the independently-phased array. The  $\beta\lambda$  cavity array of Figure 14.10a is an improvement over the independently phase array in terms of reduction of microwave hardware. There are separate power feeds but only one amplifier. Synchronization of ion motion to the rf oscillations is accomplished by varying the drift lengths between cavities. The structure of Figure 14.10b is

## Radio-frequency Linear Accelerators

a mechanically simplified version in which the two walls separating cavities are combined. In the absence of the drift tubes, the cavities have the same resonant frequency because  $\omega_{010}$  does not depend on the cavity length (Table 12.1). This reflects the fact that the capacitance of a cylindrical cavity scales as  $1/d$  while the inductance increases as  $d$ . The additional capacitance of the acceleration gap upsets the balance. It is necessary to adjust the gap geometry in different cavities to maintain a constant resonant frequency. The capacitance is determined by the drift tube diameter and the gap width. Figure 14.10b illustrates variation of drift tube diameter to compensate for increasing cavity length along the direction of acceleration. Resonant frequencies of individual cavities must be matched to within a factor of  $1/Q$  so that all cavities are excited by the driving wave; a typical requirement is 1 part in  $10^4$ . The design procedure for a cavity array often consists of the following stages:

1. Approximate dimensions are determined by analytic or computer calculations.
2. Measurements are performed on a low-power model.
3. The final cavity array is tuned at low power. Small frequency corrections can be made by deforming cavity walls (dimpling) or by adjusting tuning slugs which change the capacitance or inductance of individual cavities.

The electric fields and wall currents for the  $TM_{010}$  mode in a  $\beta\lambda$  structure are illustrated in Figure 14.9a. Note the distribution of electric field and current on the wall separating two cavities:

1. The currents in the two cavities are opposite and approximately equal; therefore, the wall carries zero net current.
2. Electric fields have equal magnitude and direction on both sides of the wall; therefore, the surface charge densities on the two sides of the wall have equal magnitude and opposite sign. There is zero net charge per area on the wall.

The field pattern is almost unchanged if the wall is removed (Fig. 14.10c). Eliminating the intervening walls leads to the drift tube accelerator of Figure 14.10c. Shaped drift tubes with increasing length along the direction of acceleration are supported by rods. The rods are located at positions of zero radial electric field; they do not seriously perturb the field distribution. An alternate view of the DTL is that it is a long cylindrical cavity with a single rf power feed to drive the  $TM_{010}$  mode; the variation of drift tube length and diameter maintains synchronization with accelerated particles and compensates the tube perturbations to maintain a constant axial electric field.

Magnetic quadrupole lenses for beam focusing are located inside the drift tubes. Power and cooling water for the magnets enter along the tube supports. The development of strong permanent magnetic materials (such as orientated samarium-cobalt) has generated interest in adjustable permanent magnet quadrupole lenses. One of the main operational problems in DTLs is

## Radio-frequency Linear Accelerators

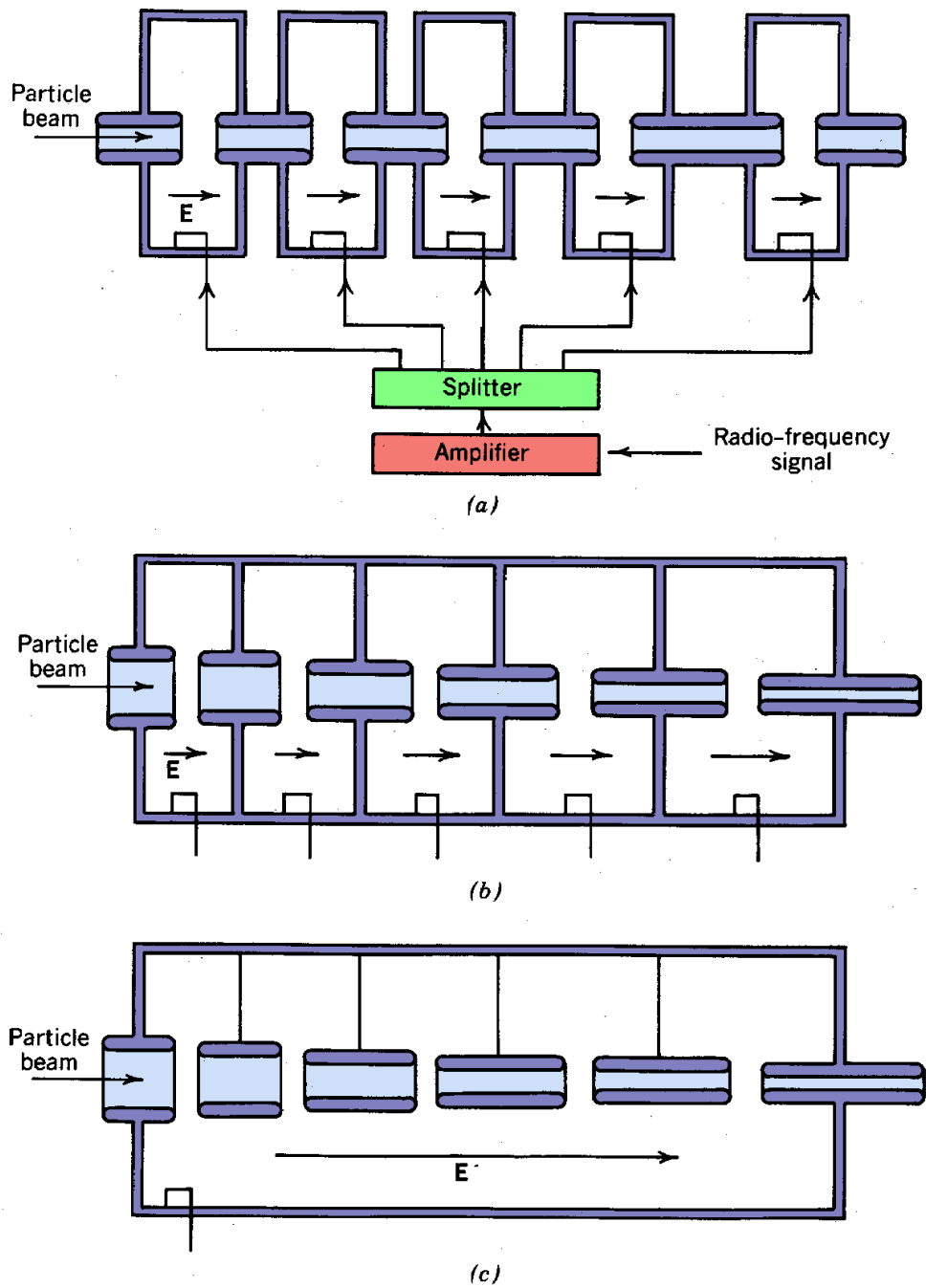
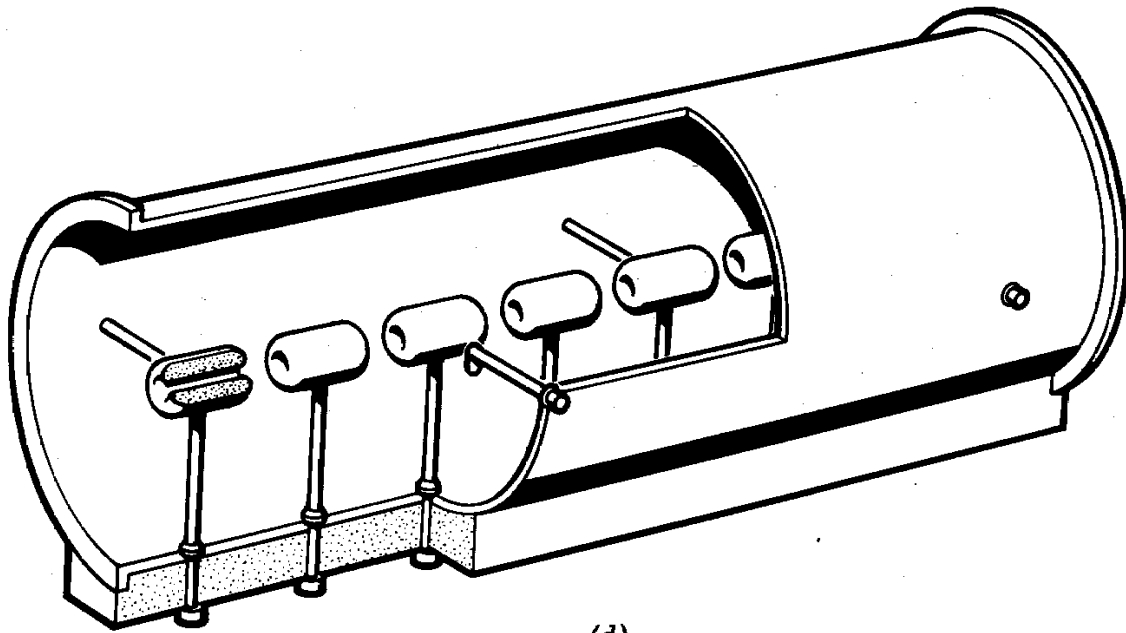


**Figure 14.10** Evolution of drift tube linear accelerator. (a) Array of resonant cavities in the  $\beta\lambda$  configuration with particle synchronization maintained by variation of distance between cavities. (b) Simplified  $\beta\lambda$  structure with synchronization by varying cavity length; uniform resonant frequency maintained by variation of drift tube and acceleration gap geometry. (c) Alvarez linac tank. (d) Drift tube linac with postcouplers to shift the frequency of undesired rf modes. (Courtesy R. Jameson, Los Alamos National Laboratory.)



(d)

Figure 14.10 (Continued).

maintaining the  $TM_{010}$  mode in a complex structure with many competing modes. Contributions of modes with transverse electric fields are particularly dangerous because they lead to beam loss. An effective solution to stabilize the rf oscillations is to incorporate tuning elements in the structure. Post couplers are illustrated in Figure 14.10d. The posts are orthogonal to the drift tube supports. They have little effect on the fundamental acceleration mode which has only longitudinal electric fields. On the other hand, the combination of drift tube support and post coupler causes a significant perturbation of other modes that have transverse electric fields. The effect is to shift the frequency of competing modes away from that of the fundamental so that they are less likely to be excited. A second purpose of the post couplers is to add periodic loading of the drift tube structures. Rotation of the post adds a small shunt capacitance to selected drift tubes. The variable loading is used to adjust the distribution of fundamental mode accelerating fields along the resonant cavity.

### 14.3 COUPLED CAVITY LINEAR ACCELERATORS

For a constrained frequency (set by rf power tube technology) and peak electric field (set by breakdown limits), a  $\beta\lambda/2$  linac has twice the average accelerating gradient as a  $\beta\lambda$  structure such as the drift tube linac. For a given beam output energy, a  $\beta\lambda/2$  accelerator is half as long as a  $\beta\lambda$  machine. Practical  $\beta\lambda/2$  geometries are based on coupled cavity arrays. In this section, we shall

## Radio-frequency Linear Accelerators

analyze the coupled cavity formalism and study some practical configurations.

To begin, we treat two cylindrical resonant cavities connected by a coupling hole (Fig. 14.11a). The cavities oscillate in the  $TM_{010}$  mode. Each cavity can be represented as a lumped element  $LC$  circuit with  $\omega_o = 1/\sqrt{LC}$  (Fig. 14.11b). Coupling of modes through an on-axis hole is capacitive. The electric field of one cavity makes a small contribution to displacement current in the other (Fig. 14.11c). In the circuit model we can represent the coupling by a capacitor  $C_c$  between the two oscillator circuits (Fig. 14.11b). If coupling is weak,  $C_c \ll C$ . Similarly, an azimuthal slot near the outer diameter of the wall between the cavities results in magnetic coupling. Some of the toroidal magnetic field of one cavity leaks into the other cavity, driving wall currents through inductive coupling (Fig. 14.11d). In the circuit model, a magnetic coupling slot is represented by a mutual inductance (Fig. 14.11e).

The following equations describe voltage and current in the circuit of Figure 14.11b:

$$-C(dV_1/dt) = I_1, \quad (14.26)$$

$$V_1 = L (dI_1/dt - di/dt), \quad (14.27)$$

$$-C(dV_2/dt) = I_2, \quad (14.28)$$

$$V_2 = L (dI_2/dt + di/dt), \quad (14.29)$$

$$i = C_c (dV_1/dt - dV_2/dt) = (C_c/C) (-I_1 + I_2). \quad (14.30)$$

When coupling is small, voltages and currents oscillate at frequency to  $\omega \cong \omega_o$  and the quantity  $i$  is much smaller than  $I_1$  or  $I_2$ . In this case, Eq. (14.30) has the approximate form

$$i \cong (-C_c \omega_o^2) (V_1 - V_2). \quad (14.31)$$

Assuming solutions of the form  $V_1, V_2 \sim \exp(j\omega t)$ , Eqs. (14.26)-(14.31) can be combined to give

$$V_1 (1 - LC\omega^2 - LC_c\omega_o^2) + V_2 (LC_c\omega_o^2) = 0, \quad (14.32)$$

$$V_1 (LC_c\omega_o^2) + V_2 (1 - LC\omega^2 - LC_c\omega_o^2) = 0. \quad (14.33)$$

Substituting  $\Omega = \omega/\omega_o$  and  $\kappa = C_c/C$ , Eqs. (14.32) and (14.33) can be written in matrix form:

$$\begin{bmatrix} 1-\Omega^2-\kappa & \kappa \\ \kappa & 1-\Omega^2-\kappa \end{bmatrix} \begin{pmatrix} V_1 \\ V_2 \end{pmatrix} = 0. \quad (14.34)$$

Radio-frequency Linear Accelerators

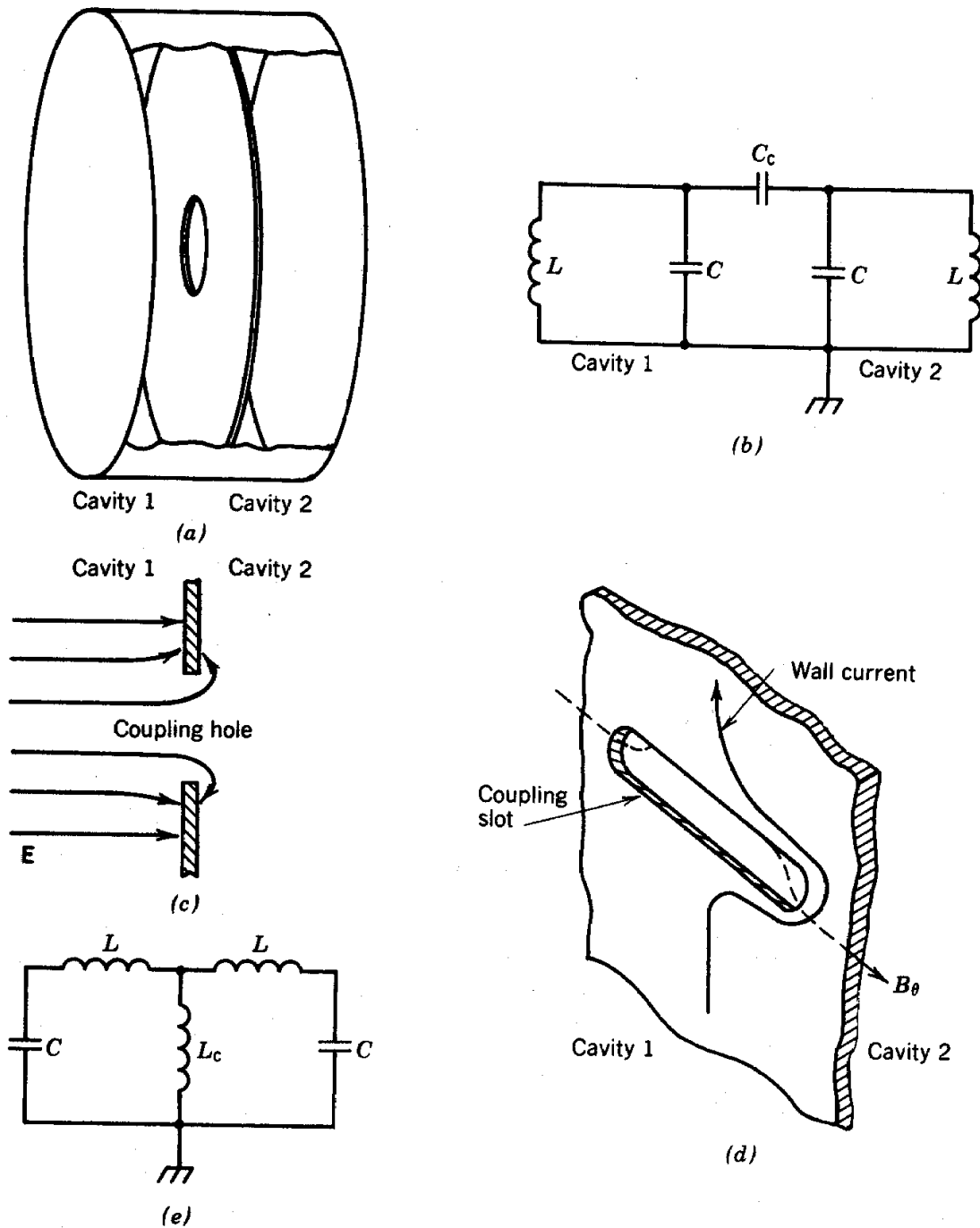


**Figure 14.11** Coupled cavities. (a) Two resonant cavities with  $TM_{010}$  modes coupled capacitively through hole on-axis. (b) Equivalent circuit model of two electrically coupled cavities. (c) Electric field distribution near coupling hole with cavity 1 excited and cavity 2 unexcited. (d) Magnetic field distribution from  $TM_{010}$  mode at azimuthal slot near outer cavity radius; cavity 1 excited, cavity 2 unexcited. (e) equivalent circuit model for two magnetically coupled cavities.

## Radio-frequency Linear Accelerators

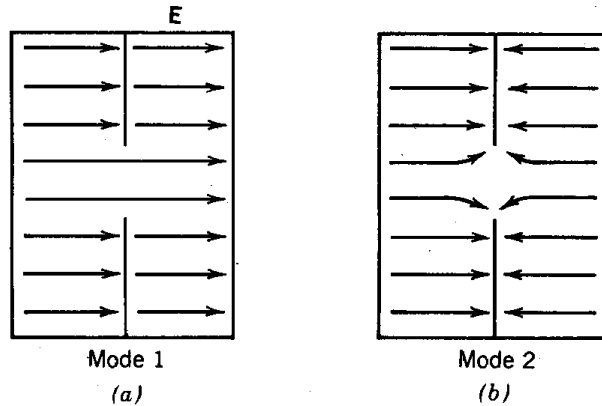


**Figure 14.12**  $TM_{010}$  modes of oscillation for two capacitively coupled cavities. (a) Electric field distribution for mode 1 (0 mode). (b) Electric field distribution for mode 2 ( $\pi$  mode).

The equations have a nonzero solution if the determinant of the matrix equals zero, or

$$(1 - \Omega^2 - \kappa^2) - \kappa^2 = 0 \quad (14.35)$$

Equation (14.35) has two solutions for the resonant frequency:

$$\Omega_1 = \omega_1/\omega_o = \sqrt{1-2\kappa}, \quad (14.36)$$

$$\Omega_2 = \omega_2/\omega_o = 1. \quad (14.37)$$

There are two modes of oscillation for the coupled two-cavity system. Substituting Eqs. (14.36) and (14.37) into Eq. (14.32) or (14.33) shows that  $V_1 = -V_2$  for the first mode and  $V_1 = V_2$  for the second. Figure 14.12 illustrates the physical interpretation of the modes. In the first mode, electric fields are aligned; the coupling hole does not influence the characteristics of the oscillation (note that  $\omega_o$  is the oscillation frequency of a single cavity without the central region). We have previously derived this result for the drift tube linac. In the second mode, the fields are anti-aligned. The interaction of electric fields near the hole cancels coupling through the aperture. A coupled two-cavity system can oscillate in either the  $\beta\lambda$  or the  $\beta\lambda/2$  mode, depending on the input frequency of the rf generator. A similar solution results with magnetic coupling.

In a coupled cavity linac, the goal is to drive a large number of cavities from a single power feed. Energy is transferred from the feed cavity to other cavities via magnetic or electric coupling. Assume that there are  $N$  identical cavities oscillating in the  $TM_{010}$  mode with uniform capacitive coupling, represented by  $C_c$ . Figure 14.13 illustrates current and voltage in the circuit model of the  $n$ th cavity. The equations describing the circuit are

## Radio-frequency Linear Accelerators

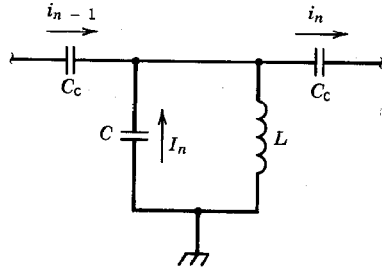


**Figure 14.13** Equivalent circuit model for array of uniform, capacitively coupled resonant cavities.

$$-C (d^2V_n/dt^2) = (dI_n/dt), \quad (14.38)$$

$$V_n = L [(dI_n/dt) - (di_n/dt) - (di_{n-1}/dt)] \quad (14.39)$$

$$di_n/dt \cong C_c \omega_o^2 (V_{n+1} - V_n). \quad (14.40)$$

The assumption of small coupling is inherent in Eq. (14.40). Taking time variations of the form  $\exp(j\omega t)$ , Eqs. (14.38)-14.40 can be combined into the single finite difference equation

$$V_{n+1} = [(1 - \Omega^2 - 2\kappa)/\kappa] V_n + V_{n-1} = 0, \quad (14.41)$$

where  $\kappa$  and  $\Omega$  are defined as above.

We have already solved a similar equation for the thin-lens array in Section 8.5. Again, taking a trial solution with amplitude variations between cells of the form

$$V_n = V_o \cos(n\mu + \phi), \quad (14.42)$$

we find that

$$\cos\mu = - (1 - \Omega^2 - 2\kappa)/2\kappa. \quad (14.43)$$

The resonant frequencies of the coupled cavity system can be determined by combining Eq. (14.43) with appropriate boundary conditions. The cavity oscillation problem is quite similar to the problem of an array of unconstrained, coupled pendula. The appropriate boundary condition is that the displacement amplitude (voltage) is maximum for the end elements of the array.

Therefore, the phase term in Eq. (14.42) is zero. Applying the boundary condition in the end cavity implies that

$$\cos[(N-1)\mu] = \pm 1. \quad (14.44)$$

## Radio-frequency Linear Accelerators

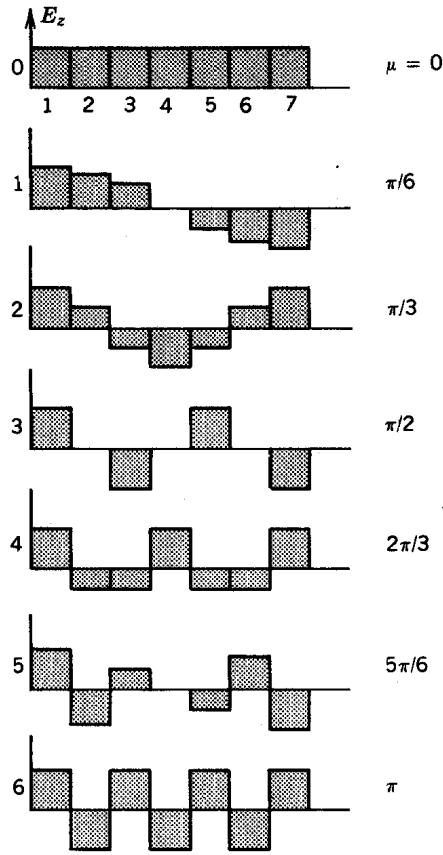


**Figure 14.14** Amplitudes of axial electric fields for allowed modes of array of seven coupled cavities.

Equation (14.44) is satisfied if

$$\mu_m = \pi m / (N-1), \quad m = 0, 1, 2, \dots, N-1. \quad (14.45)$$

The quantity  $m$  has a maximum value  $N-1$  because there can be at most  $N$  different values of  $V_n$  in the coupled cavity system.

A coupled system of  $N$  cavities has  $N$  modes of oscillation with frequencies given by

$$\Omega_m = \omega_m / \omega_o = \sqrt{1 - 2\kappa [1 - \cos(2\pi m / (N-1))].} \quad (14.46)$$

The physical interpretation of the allowed modes is illustrated in Figure 14.14. Electric field amplitudes are plotted for the seven modes of a seven-cavity system. In microwave nomenclature, the modes are referenced according to the value of  $\mu$ . The 0 mode is equivalent to a  $\beta\lambda$  structure while the  $\pi$  mode corresponds to  $\beta\lambda/2$ .

At first glance, it appears that the  $\pi$  mode is the optimal choice for a high-gradient accelerator. Unfortunately, this mode cannot be used because it has a very low energy transfer rate between

## Radio-frequency Linear Accelerators

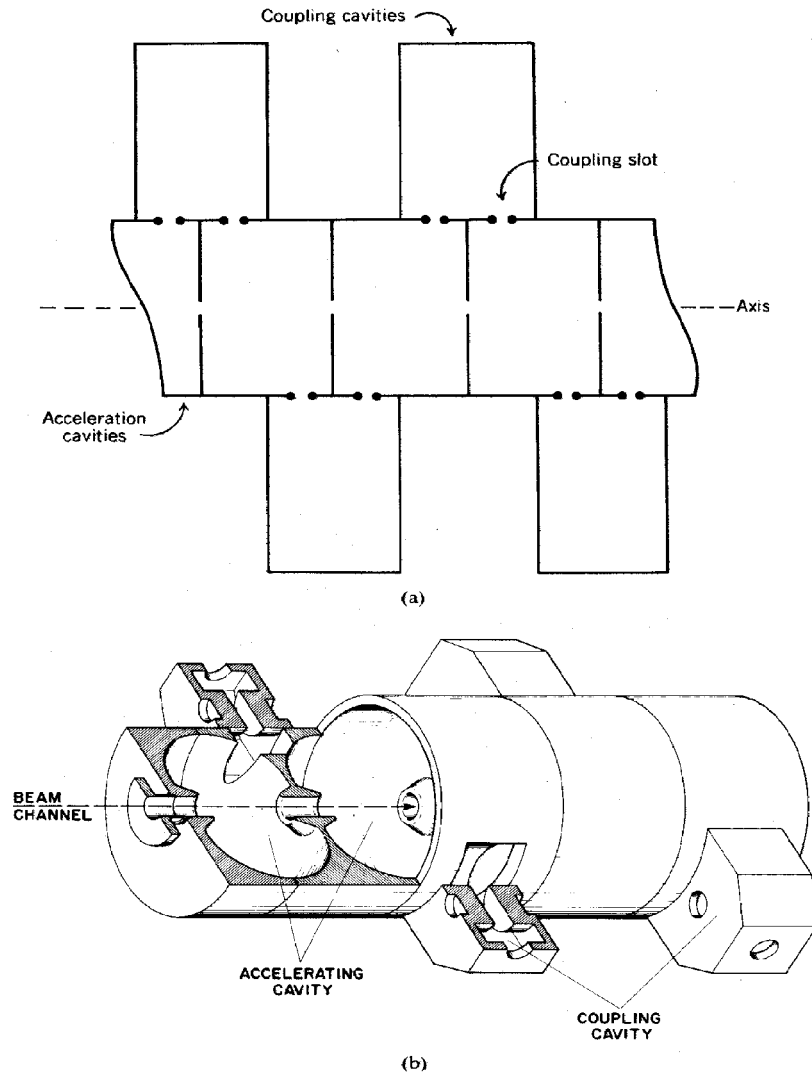


**Figure 14.15** Side-coupled linear accelerator with resonant coupling a) Schematic diagram. b) Scale cross section of LAMF accelerator cavities (Courtesy O. B. van Dyck, Los Alamos National Laboratory.)

cavities. We can demonstrate this by calculating the group velocity of the traveling wave components of the standing wave. In the limit of a large number of cavities, the positive-going wave can be represented as

$$V_+(z,t) = \exp[j(\mu z/d - \omega t)]. \quad (14.47)$$

The wavenumber  $k$  is equal to  $\mu/d$ . The phase velocity is

$$\omega/k = \omega_0 \Omega d / \mu, \quad (14.48)$$

## Radio-frequency Linear Accelerators

where  $\omega_0$  is the resonant frequency of an uncoupled cavity. For the  $\pi$  mode, Eq. (14.48) implies

$$d = (\omega/k) \pi/\omega_0 \Omega = (\beta\lambda/2)/\Omega. \quad (14.49)$$

Equation (14.49) is the  $\beta\lambda/2$  condition adjusted for the shift in resonant oscillation caused by cavity coupling.

The group velocity is

$$d\omega/dk = (\omega_0 d) d\Omega/d\mu = - (\omega_0 d) \frac{\kappa \sin\mu}{\sqrt{1-2\kappa+2\kappa\cos\mu}}.$$

Note that  $v_g$  is zero for the 0 and  $\pi$  modes, while energy transport is maximum for the  $\pi/2$  mode.

The  $\pi/2$  mode is the best choice for rf power coupling but it has a relatively low gradient because half of the cavities are unexcited. An effective solution to this problem is to displace the

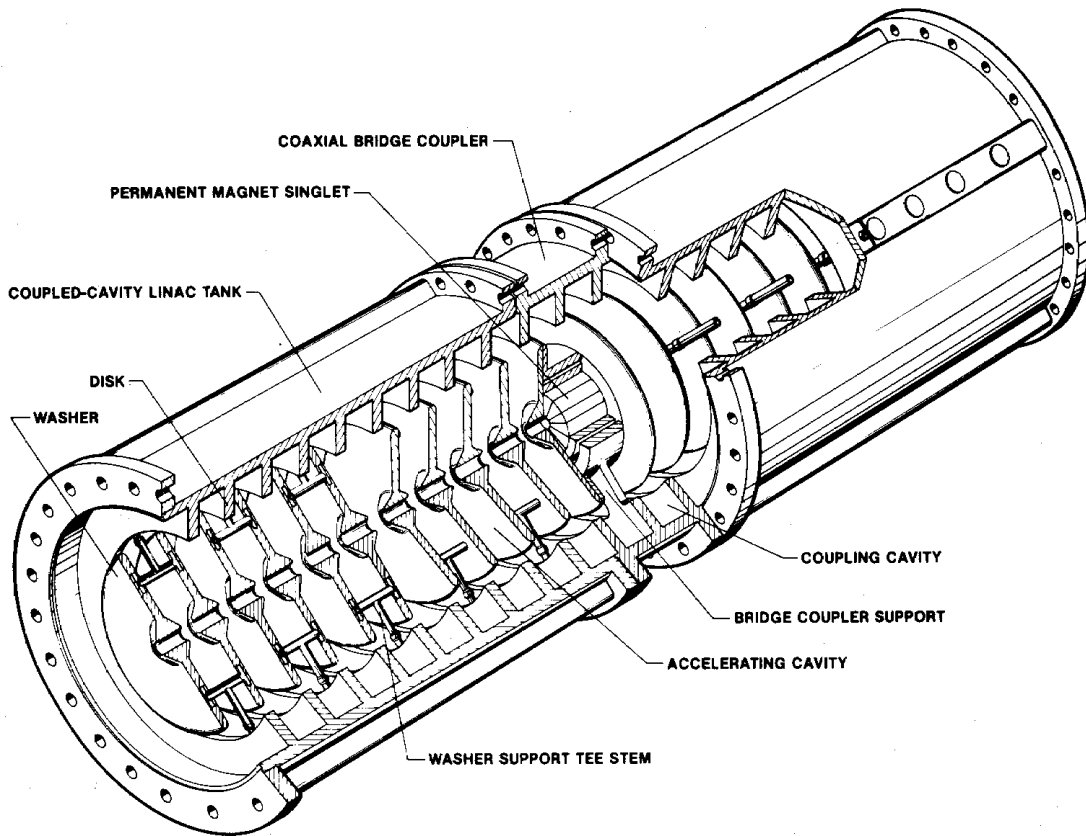
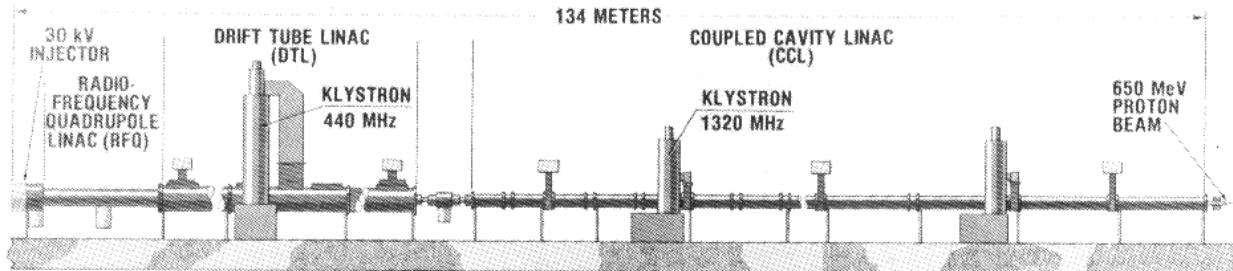


**Figure 14.16** Cutaway view of a disk-and-washer accelerator structure. (Courtesy D. Swenson, Los Alamos National Laboratory and Texas A & M University).

## PION GENERATOR FOR MEDICAL IRRADIATION (PIGMI)



### MAJOR TECHNICAL INNOVATIONS

HIGHER FREQUENCIES  
 HIGHER GRADIENTS  
 LOWER INJECTION ENERGY  
 RFQ LINAC STRUCTURE  
 POST-COUPLED DTL STRUCTURE  
 PERMANENT MAGNET QUADRUPOLE LENSES  
 DISK AND WASHER CCL STRUCTURE  
 COAXIAL BRIDGE COUPLERS  
 DISTRIBUTED MICROPROCESSOR CONTROL

### PROTON BEAM PARAMETERS

INJECTION ENERGY	30 keV
RFQ/DTL TRANSITION ENERGY	2.5 MeV
DTL/CCL TRANSITION ENERGY	125 MeV
FINAL ENERGY	650 MeV
PEAK BEAM CURRENT	28 mA
PULSE LENGTH	60 $\mu$ s
REPETITION RATE	60 Hz
AVERAGE BEAM CURRENT	100 $\mu$ A

### PROTON LINAC PARAMETERS

	FREQUENCY	KLYSTRONS	GRADIENT
RFQ & DTL SECTION	440 MHz	1	6 MV/m
CCL SECTION	1320 MHz	6	8 MV/m

Figure 14.17 Diagram and parameters of PIGMI accelerator. (Courtesy D. Swenson, Los Alamos National Laboratory and Texas A & M University).

## Radio-frequency Linear Accelerators

**TABLE 14.2 Parameters of the LAMPF Accelerator**

Accelerator length	800 m
Output beam energy	800 MeV
Output beam current	15 mA
Macropulse length	1 ms
Repetition rate	120 Hz
Duty cycle	12%
<i>Injector</i>	
Ion species	H <sup>+</sup> , H <sup>-</sup>
Maximum output current	30 mA, H <sup>+</sup>
Voltage	750 kV
Voltage generator	Cockcroft–Walton generator
Bunchers	201.25 MHz, 4-kV prebuncher, 10-kV main buncher
<i>Drift Tube Linac</i>	
Energy variation	0.75–100 MeV
Length	61.7 m
Operating frequency	201.25 MHz
Cavity $Q$	$5 \times 10^4$
rf filling time	200 $\mu$ s
Number of tanks	4
Tank diameter	0.9 m
Number of drift tubes	165
Drift tube outer diameter	0.16 m
Drift tube bore	0.75–1.5 cm
Shunt impedance	42 M $\Omega$ /m
Average axial field	1.6–2.4 MV/m peak
Maximum surface field	12 MV/m
Synchronous phase	64°
rf power units	Triode power amplifiers
Number of rf units	4
rf power rating/unit	2.7 MW
Number of focusing quadrupoles	135
Focusing magnetic field gradient	8 to 0.8 kG/cm
Focusing mode	FDFD
System normalized acceptance	$7\pi$ mm · mrad

## Radio-frequency Linear Accelerators

### *Side-Coupled Linac*

Energy variation	100–800 MeV
Total length	726.9 m
Operating frequency	805 MHz
Cavity $Q$	$1.6 \text{ to } 2.4 \times 10^4$
rf filling time	0.15 ms
Number of tanks	104
Tank length	2.9 to 7.8 m
Number of cavities	5000
Bore diameter	3.2–3.8 cm
Shunt impedance	30–42 M $\Omega$ /m
Average axial field	1.1 MV/m
Synchronous phase	64–70°
rf power units	Klystrons
Number of rf power units	44
rf power rating/unit	1.25 MW
Number of focusing quadrupoles	204
Focusing magnetic field gradient	2.2 to 3.2 kG/cm
Focusing mode	Doublets
Normalized acceptance	$17\pi \text{ mm} \cdot \text{mrad}$

---

unexcited cavities to the side and pass the ion beam through the even-numbered cavities. The result is a  $\beta\lambda/2$  accelerator with good power coupling. The side-coupled linac [See B. C. Knapp, E. A. Knapp, G. J. Lucas, and J. M. Potter, IEEE Trans. Nucl. Sci. **NS-12**, 159 (1965)] is illustrated in Figure 14.15a. Intermediate cavities are coupled to an array of cylindrical cavities by magnetic coupling slots. Low-level electromagnetic oscillations in the side cavities act to transfer energy along the system. There is little energy dissipation in the side cavities. Figure 14.15b illustrates an improved design. The side cavities are reentrant to make them more compact (see Section 12.2). The accelerator cavity geometry is modified from the simple cylinder to reduce shunt impedance. The simple cylindrical cavity has a relatively high shunt impedance because wall current at the outside corners dissipates energy while making little contribution to the cavity inductance.

The disk and washer structure (Fig. 14.16) is an alternative to the side-coupled linac. It has high shunt impedance and good field distribution stability. The accelerating cavities are defined by "washers." The washers are suspended by supports connected to the wall along a radial electric field null. The coupling cavities extend around the entire azimuth. The individual sections of the disk-and-washer structure are strongly coupled. The perturbation analysis we used to treat coupled

# Radio-frequency Linear Accelerators

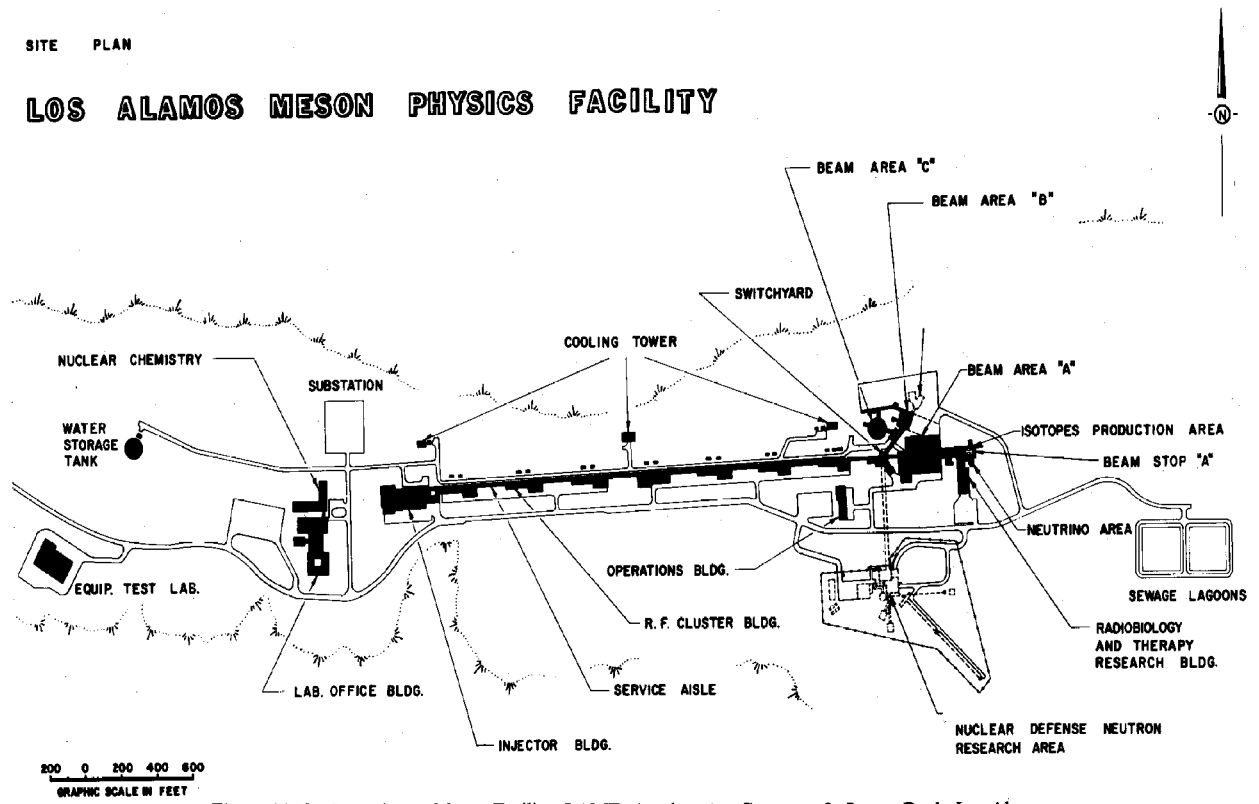


Figure 14.18 Los Alamos Meson Facility (LAMPF) Accelerator. (Courtesy, O. B. van Dyck, Los Alamos National Laboratory.)

## Radio-frequency Linear Accelerators

**TABLE 14.3 Parameters of the UNILAC<sup>a</sup>**

Accelerator length	125 m
Particle species	Variety of heavy ions, oxygen through uranium
Number of isotopes available	~ 50
Output energy ( $U$ ) <sup>b</sup>	~ 4 GeV
Energy/nucleon ( $U$ )	17 MeV
Average output current ( $U$ )	0.05 $\mu$ A
Macropulse length	5 ms
Duty cycle factor	0.25, 5 ms each 20 ms
Ion source	Penning discharge
Typical charge state ( $U$ )	+10
Typical $Z/A$ ( $U$ )	0.042
Electrostatic accelerator voltage	300 kV
Species selection	Magnetic mass separator
Wideröe accelerator, number of cavities	4
Matched entrance $\beta$	0.05
Bore diameter	0.03 m
Number of accelerating gaps	120
Total accelerating voltage	30 MV
rf frequency	27 MHz
rf power	3 MW
Energy/nucleon at exit ( $U$ )	1.4 MeV
Average charge state after stripper	+40
Alvarez accelerator, number of cavities	4
Total accelerating voltage	100 MeV
rf frequency	108 MHz = 4 $\times$ 27 MHz
rf power	5 MW
Number of cavities and rf amplifiers, independently phased array for beam energy variation	17
Accuracy of final beam energy	0.1%
Micropulse length	0.2 to 4 ns

<sup>a</sup>Gesellschaft für Schwerionenforschung.

<sup>b</sup>Parameters quoted for uranium ions.

## Radio-frequency Linear Accelerators

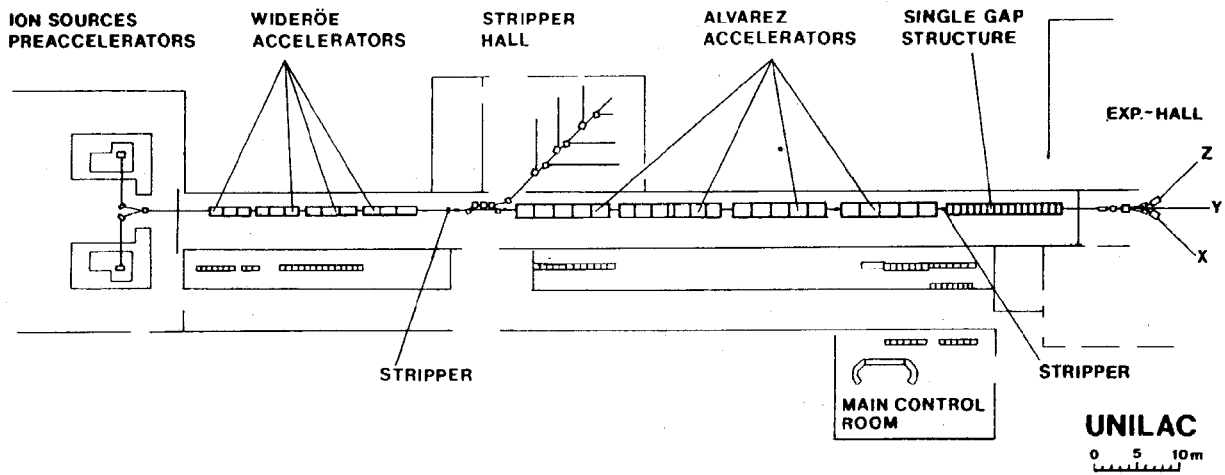


Figure 14.19 UNILAC heavy-ion linear accelerator. (Courtesy D. Böhne, Gesellschaft für Schwerionenforschung).

## Radio-frequency Linear Accelerators

cavities is inadequate to determine the resonant frequencies of the disk-and-washer structure. The development of strongly-coupled cavity geometries results largely from the application of digital computers to determine normal modes.

In contrast to electron accelerators, ion linear accelerators may be composed of a variety of acceleration structures. Many factors must be considered in choosing the accelerating components, such as average gradient, field stability, shunt impedance, fabrication costs, and beam throughput. Energy efficiency has become a prime concern; this reflects the rising cost of electricity as well as an expansion of interest in the accelerator community from high-energy physics to commercial applications. Figure 14.17 shows an accelerator designed for medical irradiation. Three types of linear accelerators are used. Notice that the factor of 4 increase in frequency between the low- and high-energy sections. Higher frequency gives higher average gradient. The beam micro-bunches are compressed during acceleration in the drift-tube linac (see Section 13.4) and are matched into every fourth bucket of the coupled cavity linac.

Parameters of the Los Alamos Meson Facility (LAMF) accelerator are listed in Table 14.2. The machine, illustrated in Figure 14.18, was designed to accelerate high-current proton beams for meson production. Parameters of the UNILAC are listed in Table 14.3. The UNILAC, illustrated in Figure 14.19, accelerates a wide variety of highly ionized heavy ions for nuclear physics studies.

### 14.4 TRANSIT-TIME FACTOR, GAP COEFFICIENT, AND RADIAL DEFOCUSING

The diameter of accelerator drift tubes and the width of acceleration gaps cannot be chosen arbitrarily. The dimensions are constrained by the properties of electromagnetic oscillations. In this section, we shall study three examples of rf field properties that influence the design of linear accelerators: the transit-time factor, the gap coefficient, and the radial defocusing forces of traveling waves.

The *transit-time factor* applies mainly to drift tube accelerators with narrow acceleration gaps. The transit-time factor is important when the time for particles to cross the gap is comparable to or longer than the half-period of an electromagnetic oscillation. If  $d$  is the gap width, this condition can be written

$$d/v_s \geq \pi/\omega. \quad (14.51)$$

where  $v_s$  is the synchronous velocity. In this limit, particles do not gain energy  $eE_o d \sin\omega t$ . Instead, they are accelerated by a time-averaged electric field smaller than  $E_o \sin\omega t$ .

Assume that the gap electric field has time variation

$$E_z(r,z,t) = E_o \cos(\omega t + \phi). \quad (14.52)$$

## Radio-frequency Linear Accelerators

The longitudinal equation of motion for a particle crossing the gap is

$$dp_z/dt = qE_o \sin(\omega t + \phi). \quad (14.53)$$

Two assumptions simplify the solution of Eq. (14.53).

1. The time  $t = 0$  corresponds to the time that the particle is at the middle of the gap.
2. The change in particle velocity over the gap is small compared to  $v_s$ .

The quantity  $\phi$  is equivalent to the particle phase in the limit of a gap of zero thickness (see Fig. 13.1). The change in longitudinal motion is approximately

$$\Delta p_z \cong qE_o \int_{-d/2v_s}^{d/2v_s} \cos(\omega t + \phi) dt = qE_o \int_{-d/2v_s}^{d/2v_s} (\cos \omega t \sin \phi - \sin \omega t \cos \phi) dt. \quad (14.54)$$

Note that the term involving  $\sin \omega t$  is an odd function; its integral is zero. The total change in momentum is

$$\Delta p_z \cong (2qE_o/\omega) \sin(d/2v_s) \sin \phi. \quad (14.55)$$

The momentum gain of a particle in the limit  $d \Rightarrow 0$  is

$$\Delta p_o = qE_o \sin \phi (d/v_s). \quad (14.56)$$

The ratio of the momentum gain for a particle in a gap with nonzero width to the ideal thin gap is defined as the transit-time factor:

$$T_f = \Delta p/\Delta p_o = \sin(\omega d/2v_s)/(\omega d/2v_s). \quad (14.57)$$

The transit-time factor is also approximately equal to the ratio of energy gain in a finite-width gap to that in a zero-width gap.

Defining a particle transit time as  $\Delta t = d/v_s$ , Eq. (14.57) can be rewritten

$$T_f = \sin(\omega \Delta t/2)/(\omega \Delta t/2). \quad (14.58)$$

The transit-time factor is plotted in Figure 14.20 as a function of  $\omega \Delta t$ .

As an application example, consider acceleration of 5 MeV Cs<sup>+</sup> ions in a Wideröe accelerator operating at  $f = 2$  MHz. The synchronous velocity is  $2.6 \times 10^6$  m/s. The transit time across a 2-cm gap is  $\Delta t = 7.5$  ns. The quantity  $\omega \Delta t$  equals 0.95; the transit-time factor is 0.963. If the

## Radio-frequency Linear Accelerators

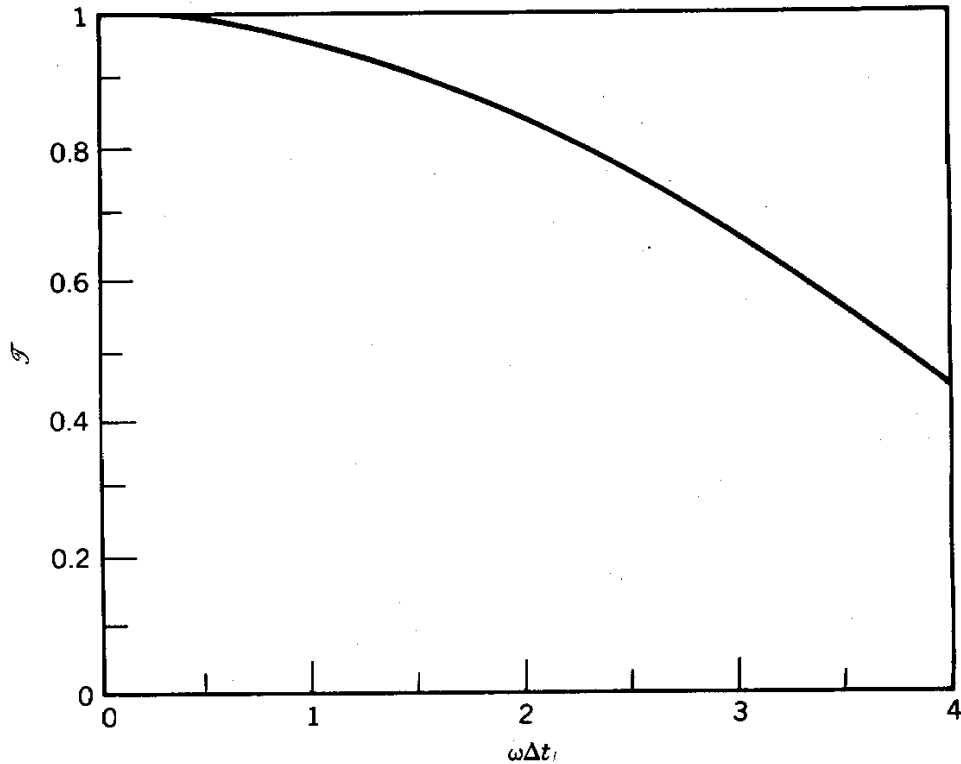


**Figure 14.20** Transit-time factor as function of  $\omega \Delta t$ .

synchronous phase is  $60^\circ$  and the peak gap voltage is 100 kV, the cesium ions gain an average energy of  $(100)(0.963)(\sin 60^\circ) = 83$  keV per gap.

The *gap coefficient* characterizes the radial variation of accelerating fields across the dimension of the beam. Variations in  $E_z$  lead to a spread in beam energy; particles with large-amplitude transverse oscillations gain a different energy than particles on the axis. Large longitudinal velocity spread is undesirable for research applications and may jeopardize longitudinal confinement in rf buckets. We shall first perform a non-relativistic derivation because the gap coefficient is primarily of interest in linear ion accelerators.

The slow-wave component of electric field chiefly responsible for particle acceleration has the form

$$E_z(0, z, t) = E_o \sin(\omega t - \omega z/v_s). \quad (14.59)$$

As discussed in Section 13.3, a slow wave appears to be an electrostatic field with no magnetic field when observed in a frame moving at velocity  $v_s$ . The magnitude of the axial electric field is unchanged by the transformation. The on-axis electric field in the beam rest frame is

$$E_z(0, z') = -E_o \sin(2\pi z'/\lambda'), \quad (14.60)$$

## Radio-frequency Linear Accelerators

where  $\lambda'$  is the wavelength in the rest frame. In the nonrelativistic limit,  $\lambda = \lambda'$  so that

$$\lambda' = 2\pi v_s / \omega. \quad (14.61)$$

The origin and sign convention in Eq. (14.60) are chosen so that a positive particle at  $z' = 0$  has zero phase. In the limit that the beam diameter is small compared to  $\lambda'$ , the electrostatic field can be described by the paraxial approximation. According to Eq. (6.5), the radial electric field is

$$E_r(r', z') \cong (r'/2) (2\pi/\lambda') E_o \cos(2\pi z'/\lambda'). \quad (14.62)$$

The equation  $\nabla \times \mathbf{E} = 0$  implies that

$$E_r(r', z') \cong -E_o [1 - (\pi r'/\lambda')^2 \sin(2\pi z'/\lambda')] \quad (14.63)$$

The energy gain of a particle at the outer radius of the beam ( $r_b$ ) is reduced by a factor proportional to the square of the gap coefficient:

$$\Delta T/T \cong - (\pi r_b/\lambda')^2. \quad (14.64)$$

The gap coefficient must be small compared to unity for a small energy spread. Equation (14.64) sets a limit on the minimum wavelength of electromagnetic waves in terms of the beam radius and allowed energy spread:

$$\lambda > \pi r_b / \sqrt{\Delta T/T}. \quad (14.65)$$

As an example, consider acceleration of a 10-MeV deuteron beam of radius 0.01m. To obtain an energy spread less than 1%, the wavelength of the slow wave must be greater than 0.31 m. Using a synchronous velocity of  $3 \times 10^7$  m/s, the rf frequency must be lower than  $f < 100$  MHz.

This derivation can also be applied to demonstrate radial defocusing of ion beams by the fields of a slow wave. Equation (14.62) shows that slow waves must have radial electric fields. Note that the radial field is positive in the range of phase  $0^\circ < \phi < 90^\circ$  and negative in the range  $90^\circ < \phi < 180^\circ$ . Therefore, the rf fields radially defocus particles in regions of axial stability. The radial forces must be compensated in ion accelerators by transverse focusing elements, usually magnetic quadrupole lenses. The stability properties of a slow wave are graphically illustrated in Figure 14.21. The figure shows three-dimensional variations of the electrostatic confinement potential (see Section 13.3) of an accelerating wave viewed in the wave rest frame. It is clear that there is no position in which particles have stability in both the radial and axial directions.

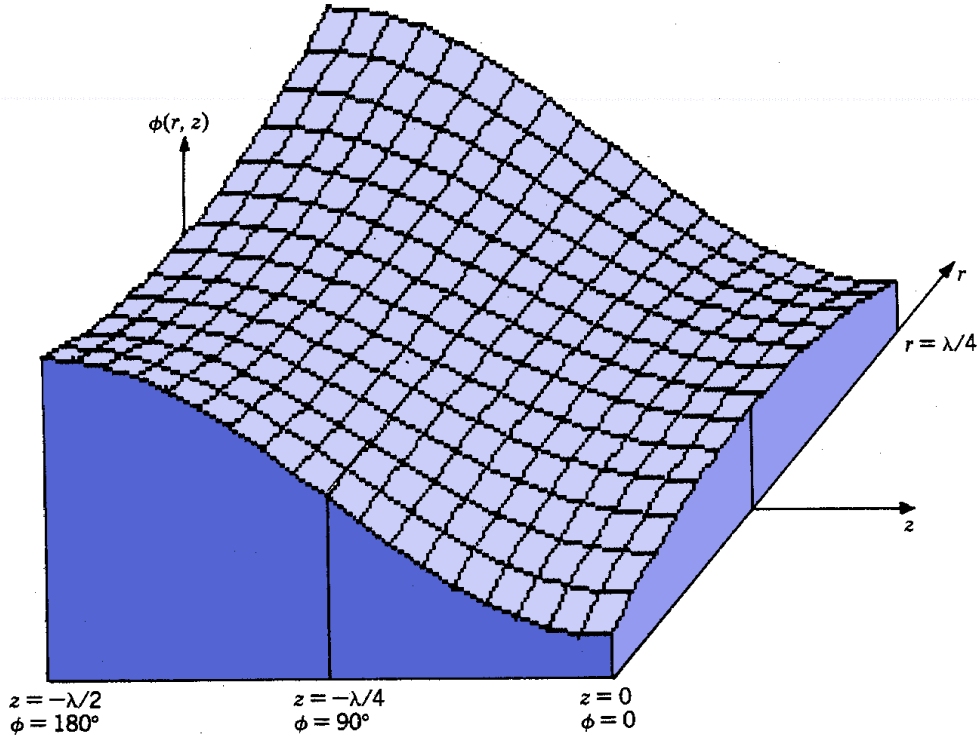


**Figure 14.21** Three-dimensional view of variations of the electrostatic potential of a slow wave viewed in the wave rest frame.

The problems of the gap coefficient and radial defocusing are reduced greatly for relativistic particles. For a relativistic derivation, we must include the fact that the measured wavelength of the slow wave is not the same in the stationary frame and the beam rest frame. Equation (2.23) implies that the measurements are related by

$$\lambda = \lambda'/\gamma, \quad (14.66)$$

where  $\gamma$  is the relativistic factor,  $\gamma = 1/\sqrt{1 - (v_s/c)^2}$ . Again, primed symbols denote the synchronous particle rest frame.

The radial and axial fields in the wave rest frame can be expressed in terms of the stationary frame wavelength:

$$E_r'(r', z') \cong E_o' (-r'/2) (2\pi/\gamma\lambda) \cos(2\pi z'/\gamma\lambda), \quad (14.67)$$

$$E_z'(r', z') \cong E_o' [1 - (\pi r'/\gamma\lambda)^2] \sin(2\pi z'/\gamma\lambda). \quad (14.68)$$

Note that the peak value of axial field is unchanged in a relativistic transformation ( $E_o' = E_o$ ). Transforming Eq. (14.68) to the stationary frame, we find that

## Radio-frequency Linear Accelerators

$$E_z(r,z) = E_o [1 - (\pi r/\gamma\lambda)^2] \sin(2\pi z/\lambda), \quad (14.69)$$

with the replacement  $r = r'$ ,  $z = z'/\gamma$ . Equation (14.69) differs from Eq. 14.63 by the  $\gamma$  factor in the denominator of the gap coefficient. The radial variation of the axial accelerating field is considerably reduced at relativistic energies.

The transformation of radial electric fields to the accelerator frame is more complicated. A pure radial electric field in the rest frame corresponds to both a radial electric field and a toroidal magnetic field in the stationary frame:

$$E_r' = \gamma (E_r + v_z B_\theta). \quad (14.70)$$

Furthermore, the total radial force exerted by the rf fields on a particle is written in the stationary frame as

$$F_r = q (E_r + v_z B_\theta). \quad (14.71)$$

The net radial defocusing force in the stationary frame is

$$F_r = [E_o (r/2) (2\pi/\lambda) \cos(2\pi z/\lambda)]/\gamma^2. \quad (14.72)$$

Comparison with Eq. (14.62) shows that the defocusing force is reduced by a factor of  $\gamma^2$ . Radial defocusing by rf fields is negligible in high-energy electron linear accelerators.

## 14.5 VACUUM BREAKDOWN IN RF ACCELERATORS

Strong electric fields greater than 10 MV/m can be sustained in rf accelerators. This results partly from the fact that there are no exposed insulators in regions of high electric field. In addition, rf accelerators are run at high duty cycle, and it is possible to condition electrodes to remove surface whiskers. The accelerators are operated for long periods of time at high vacuum, minimizing problems of surface contamination on electrodes.

Nonetheless, there are limits to the voltage gradient set by resonant particle motion in the oscillating fields. The process is illustrated for electrons in an acceleration gap in Figure 14.22. An electron emitted from a surface during the accelerating half-cycle of the rf field can be accelerated to an opposing electrode. The electron produces secondary electrons at the surface. If the transit time of the initial electron is about one-half that of the rf period, the electric field will be in a

## Radio-frequency Linear Accelerators

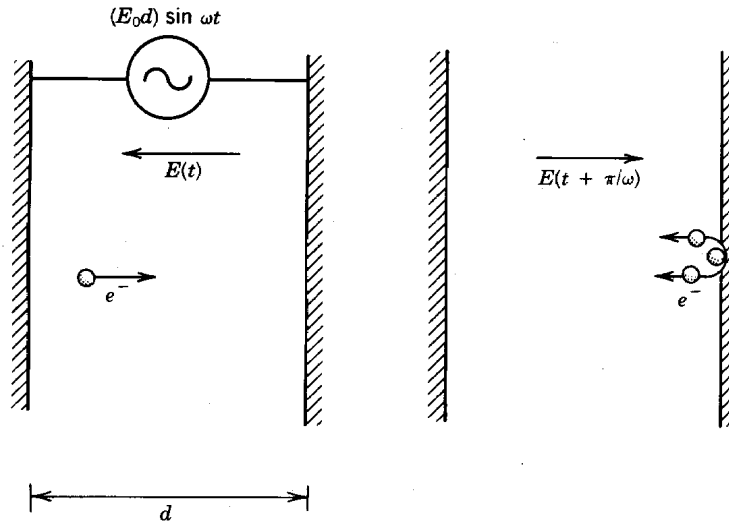


**Figure 14.22** Geometry for calculating electron multipactoring. Electron field indicated at times of electron emission and electron collision with opposing electrode.

direction to accelerate the secondary electrons back to the first surface. If the secondary electron coefficient  $\delta$  is greater than unity, the electron current grows. Table 14.4 shows maximum secondary electron coefficients for a variety of electrode materials. Also included are the incident electron energy corresponding to peak emission and to  $\delta = 1$ . Emission falls off at a higher electron energy. Table 14.4 gives values for clean, outgassed surfaces. Surfaces without special cleaning may have a value of  $\delta$  as high as 4.

The resonant growth of electron current is called multipactoring, implying multiple electron impacts. Multipactoring can lead to a number of undesirable effects. The growing electron current absorbs rf energy and may clamp the magnitude of electric fields at the multipactoring level. Considerable energy can be deposited in localized regions of the electrodes, resulting in outgassing or evaporation of material. This often leads to a general cavity breakdown.

**TABLE 14.4 Secondary Electron Coefficient**

Metal	$d$ (electrons per incident electron)	Electron Energy at $\delta_{\max}$ (eV)	Electron Energy for $\delta = 1$ (eV)
Al	1.9	220	35
Au	1.1	330	160
Cu	1.3	240	100
Fe	1.3	350	120
Mo	1.3	360	120
Ni	1.3	460	160
W	1.45	700	200

## Radio-frequency Linear Accelerators

Conditions for electron multipactoring can be derived easily for the case of a planar gap with electrode spacing  $d$ . The electric field inside the gap is assumed spatially uniform with time variation given by

$$E(x,t) = -E_o \sin(\omega t + \phi). \quad (14.73)$$

The non-relativistic equation of motion for electrons is

$$m_e (d^2x/dt^2) = eE_o \sin(\omega t + \phi). \quad (14.74)$$

The quantity  $\phi$  represents the phase of the rf field at the time an electron is produced on an electrode. Equation (14.74) can be integrated directly. Applying the boundary conditions that  $x = 0$  and  $dx/dt = 0$  at  $t = 0$ , we find that

$$x = - (eE_o/m_e\omega^2) [\omega t \cos\phi + \sin\phi - \sin(\omega t + \phi)]. \quad (14.75)$$

Resonant acceleration occurs when electrons move a distance  $d$  in a time interval equal to an odd number of rf half-periods. When this condition holds, electrons emerging from the impacted electrode are accelerated in the  $-x$  direction; they follow the same equation of motion as the initial electrons. The resonance condition is

$$\Delta t = (2n+1) (\pi/\omega). \quad (14.76)$$

for  $n = 0, 1, 2, 3, \dots$ . Combining Eqs. (14.75) and (14.76), the resonant condition can be rewritten

$$d = - (eE_o/m_e\omega^2) [(2n+1) \pi \cos\phi + 2\sin\phi], \quad (14.77)$$

because  $\sin(\omega\Delta t + \phi) = -\sin\phi$ . Furthermore, we can use Eq. (14.75) to find the velocity of electrons arriving at an electrode:

$$v_x(x=d) = - (2eE_o/m_e\omega^2) \cos\phi. \quad (14.78)$$

The solution of Eq. (14.74) is physically realizable only for particles leaving the initial electrode within a certain range of  $\phi$ . First, the electric field must be negative to extract electrons from the surface at  $t = 0$ , or  $\sin\phi > 0$ . A real solution exists only if electrons arrive at the opposite electrode with positive velocity, or  $\cos\phi > 0$ . These two conditions are met in the phase range

$$0 < \phi < \pi/2. \quad (14.79)$$

## Radio-frequency Linear Accelerators

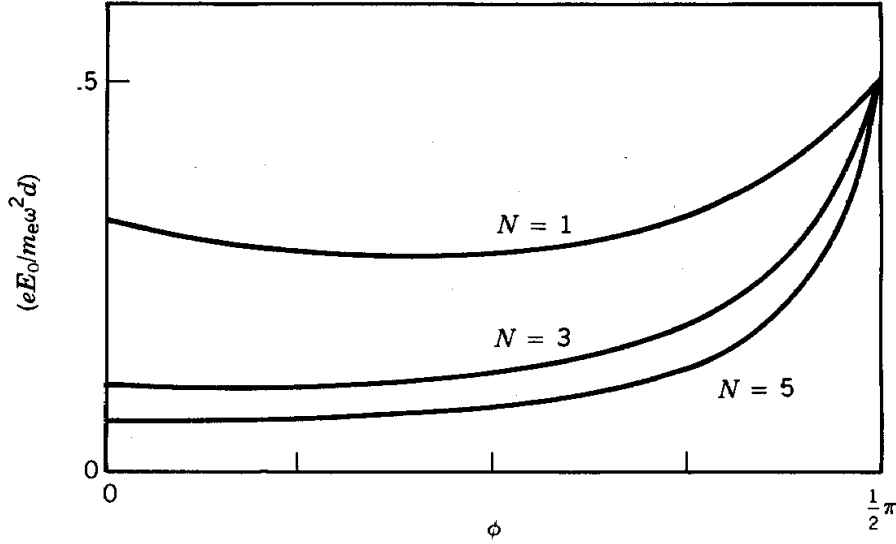


**Figure 14.23** Conditions for electron multipactoring in planar gap of width  $d$ . Normalized resonant electric field,  $eE_0/m_e\omega^2d$ , versus rf phase at time of electron emission:  $E_0$ , peak electric field;  $\omega$ , rf angular frequency;  $N$ , number of rf half-periods during electron transit.

Figure 14.23 is a plot of Eq. (14.77) showing the breakdown parameter  $(eE_0/m_e\omega^2d)$  versus the rf phase at which electrons leave the surface. Electron resonance is possible, in principle, over a range of gap voltage from 0 to  $V = m_e\omega^2d^2/2e$ .

Electron multipactoring is a significant problem in the low-energy sections of linear ion accelerators. Consider, for example, an acceleration gap for 2-MeV protons. Assume that the proton transit time  $\Delta t$  is such that  $\omega\Delta t = 1$ . This implies that  $\omega d = \beta c$ . Substituting the above condition in Eq. (14.78) and taking the  $n = 0$  resonance condition, the electron energy at impact is  $E_c = (2/\pi^2) (\beta\cos\phi)^2 (m_e c^2)$ . The quantity  $\beta$  equals 0.065 for 2-MeV protons. The peak electron energy occurs when  $\cos\phi = 1$  ( $\phi = 0$ ); for the example it is 440 eV. Table 14.4 shows that this value is close to the energy of peak secondary electron emission. Electrons emitted at other phases arrive at the opposing electron with lower energy; therefore, they are not as likely to initiate a resonant breakdown. For this reason, the electron multipactoring condition is often quoted as

$$V_o = (d\omega)^2 m_e / \pi e = (2\pi d/\lambda)^2 (m_e c^2) / \pi e. \quad (14.80)$$

Equation (14.80) is expressed in terms of  $\lambda$ , the vacuum wavelength of the rf oscillations.

Electron multipactoring for the case quoted is probably not significant for values of  $n$  greater than zero because the peak electron energy is reduced by a factor of about  $2n^2$ . Therefore, breakdowns are usually not observed until the gap reaches a voltage level near that of Eq. (14.80). For an rf frequency  $f = 400$  MHz, an acceleration gap 0.8 cm in width has  $\omega\Delta t = 1$  for 2-MeV

## Radio-frequency Linear Accelerators

protons. This corresponds to a peak voltage of 730 V. At higher field levels, the resonance condition can be met over longer pathlengths at higher field stresses. This corresponds to high-energy electrons, which generally have secondary emission coefficients less than unity. Therefore, with clean surfaces it is possible to proceed beyond multipactoring by raising the rf electric field level rapidly. This may not be the case with contaminated electrodes; surface effects contribute much of the mystery and aggravation associated with rf breakdown.

The ultimate limits for rf breakdown in clean acceleration gaps were investigated experimentally by Kilpatrick [W.D. Kilpatrick, "Criterion for Vacuum Sparking to Include Both RF and DC," University of California Radiation Laboratory, UCRL-2321, 1953]. The following formula is consistent with a wide variety of observations:

$$V_K = (2\pi d/\lambda)^2 (m_p c^2)/\pi e. \quad (14.81)$$

Note that Eq. (14.81) is identical to Eq. 14.80 with the replacement of the electron mass by that of the proton. The Kilpatrick voltage limit is about a factor of 2000 times the electron multipactoring condition. The similarity of the equations suggests proton multipactoring as a mechanism for high-voltage rf breakdown. The precise mechanisms of proton production on electrode surfaces are unknown. Proton production may be associated with thin surface coatings. Present research on extending rf systems past the Kilpatrick limit centers on the use of proton-free electrodes.

## 14.6 RADIO-FREQUENCY QUADRUPOLE

The rf quadrupole [I.M. Kapchinskii and V. A. Teplyakov, *Priboty i Teknika Eksperimenta* **2**, 19 (1970); R. H. Stokes, K. R. Crandall, J. E. Stovall, and D. A. Swenson, *IEEE Trans. Nucl. Sci.* **NS-26**, 3469 (1979)] is an ion accelerator in which both acceleration and transverse focusing are performed by rf fields. The derivations of Section 14.4 (showing lack of absolute stability in an rf accelerator) were specific to a cylindrical system; the fields in an RFQ are azimuthally asymmetric. There is no moving frame of reference in which RFQ fields can be represented as an electrostatic distribution. We shall see that the electric fields in the RFQ consist of positive and negative traveling waves; the positive wave continually accelerates ions in the range of stable phase. The beam is focused by oscillating transverse electric field components. These fields provide net beam focusing if the accelerating fields are not too high.

The major application of the RFQ is in low-energy ion acceleration. In the past, low-velocity ion acceleration presented one of the main technological difficulties for high-flux accelerators. A conventional ion beam injector consists of an ion source floating at high voltage and an electrostatic acceleration column. Space charge forces are strong for low-velocity ion beams; this

## Radio-frequency Linear Accelerators

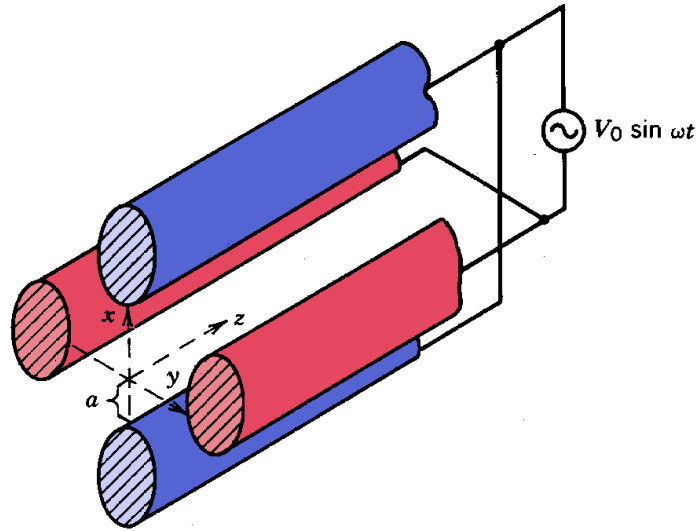


**Figure 14.24** Radio-frequency electrostatic quadrupole for transverse confinement of charged particles.

fact motivates the choice of a high injection voltage, typically greater than 1 MV. The resulting system with adequate insulation occupies a large volume. The extracted beam must be bunched for injection into an rf accelerator. This implies long transport sections with magnetic quadrupole lenses. Magnetic lenses are ineffective for focusing low-energy ion beams, so that flux limits are low.

In contrast, the RFQ relies on strong electrostatic focusing in a narrow channel; this allows proton beam current in the range of 10 to 100 mA. An additional advantage of the RFQ is that it can combine the functions of acceleration and bunching. This is accomplished by varying the geometry of electrodes so that the relative magnitudes of transverse and longitudinal electric fields vary through the machine. A steady-state beam can be injected directly into the RFQ and reversibly bunched while it is being accelerated.

The quadrupole focusing channel treated in Chapter 8 has static fields with periodically alternating field polarity along the beam axis. In order to understand the RFQ, we will consider the geometry illustrated in Figure 14.24. The quadrupole electrodes are axially uniform but have time-varying voltage of the form  $V_0 \sin \omega t$ . It is valid to treat the fields near the axis in the electrostatic limit if  $a \ll c/\omega$ , where  $a$  is the distance between the electrodes and the axis. In this case, the electric fields are simply the expressions of Eqs. (4.22) and (4.23) multiplied by  $\sin \omega t$ :

$$E_x(x,y,z,t) = (E_0 x/a) \sin \omega t, \quad (14.82)$$

$$E_y(x,y,z,t) = - (E_0 y/a) \sin \omega t. \quad (14.83)$$

The oscillating electric fields near the axis are supported by excitation of surrounding microwave structures. Off-axis fields must be described by the full set of Maxwell equations.

## Radio-frequency Linear Accelerators

The non-relativistic equation for particle motion in the x direction is

$$m (d^2x/dt^2) = (qE_0 x/a) \sin\omega t. \quad (14.84)$$

Equation (14.84) can be solved by the theory of the Mathieu equations. We will take a simpler approach to arrive at an approximate solution. Assume that the period for a transverse particle orbit oscillation is long compared to  $2\pi/\omega$ . In this limit, particle motion has two components; a slow betatron oscillation (parametrized by frequency  $\Omega$ ) and a rapid small-amplitude motion at frequency  $\omega$ . We shall seek a solution by iteration using the trial solution

$$x(t) = x_0 \sin\Omega t + x_1 \sin\omega t. \quad (14.85)$$

where

$$x_1 \ll x_0, \quad (14.86)$$

$$\Omega \ll \omega, \quad (14.87)$$

$$\Omega^2 x_0 \ll \omega^2 x_1. \quad (14.88)$$

Substituting Eq. (14.85) into Eq. (14.84), we find that

$$-\Omega^2 x_0 \sin\Omega t - \omega^2 x_1 \sin\omega t = (qE_0/ma) \sin\omega t (x_0 \sin\Omega t + x_1 \sin\omega t). \quad (14.89)$$

The first term on the left-hand side and the second term on the right-hand side of Eq. (14.89) are dropped according to Eqs. (14.88) and (14.86). The result is an equation for the high-frequency motion:

$$-\omega^2 x_1 \cong [qE_0 x_0 \sin(\Omega t)/a]/m$$

or

$$x_1 \cong - [qE_0 x_0 \sin(\Omega t)/a]/m\omega^2. \quad (14.90)$$

The second step is to substitute Eq. (14.90) into Eq. (14.84) and average over a fast oscillation period to find the long-term motion. Terms containing  $\sin\omega t$  average to zero. The remaining terms imply the following approximate equation for  $x_0$ :

## Radio-frequency Linear Accelerators

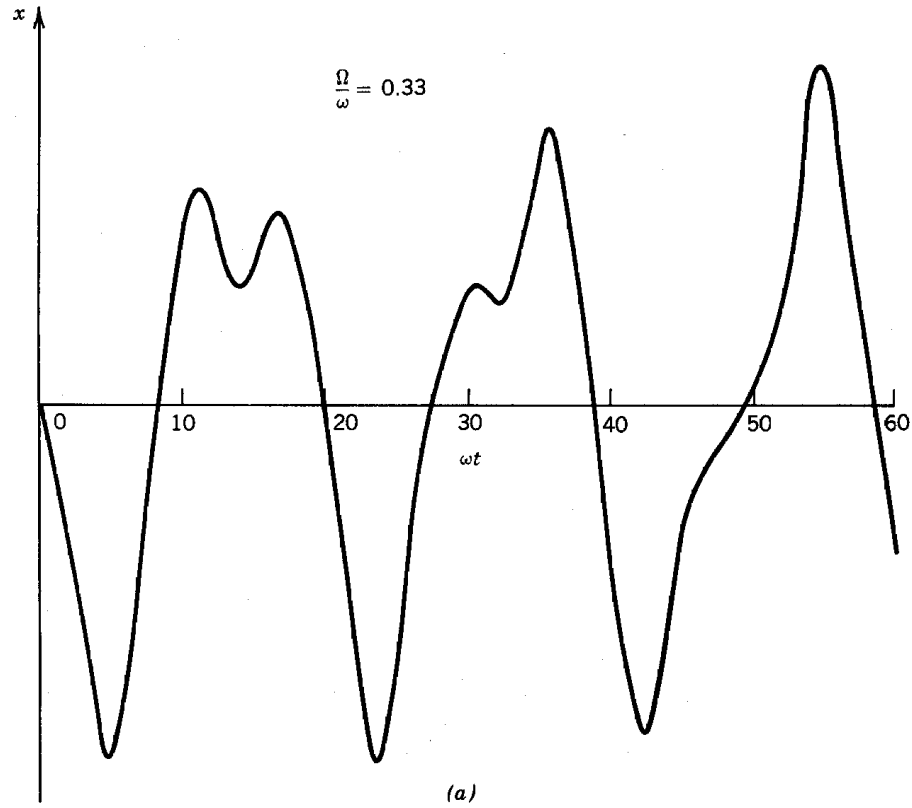


**Figure 14.25** Numerical solutions for transverse motion of non-relativistic particle in oscillating electrostatic quadrupole field:  $\Omega = (qE_0/m_0a\omega)/\sqrt{2}$ ;  $E_0$ , peak electric field at electrode tip;  $a$ , distance from axis to electrode tip;  $m_0$ , particle rest mass;  $\omega$ , rf angular frequency. (a)  $\Omega/\omega = 0.33$ . (b)  $\Omega/\omega = 0.1$ .

$$-\Omega^2 x_0 \sin\Omega t \cong - (qE_0/ma)^2 (x_0 \sin\Omega t) \overline{(\sin^2\omega t)}/\omega^2, \quad (14.91)$$

where  $\overline{\sin^2\omega t}$  denotes the average over a time  $2\pi/\omega$ . Equation (14.91) implies that  $\Omega$  has the real value

$$\Omega = (eE_0/ma\omega)/\sqrt{2}. \quad (14.92)$$

The long-term motion is oscillatory; the time-varying quadrupole fields provide net focusing. Numerical solutions to Eq. (14.84) are plotted in Figure 14.25 for  $\omega=3\Omega$  and  $\omega=10\Omega$ . The phase relationship of Eq. (14.90) guarantees that particles are at a larger displacement when the fields are focusing. This is the origin of the average focusing effect. Orbit solutions in the y direction are similar.

## Radio-frequency Linear Accelerators

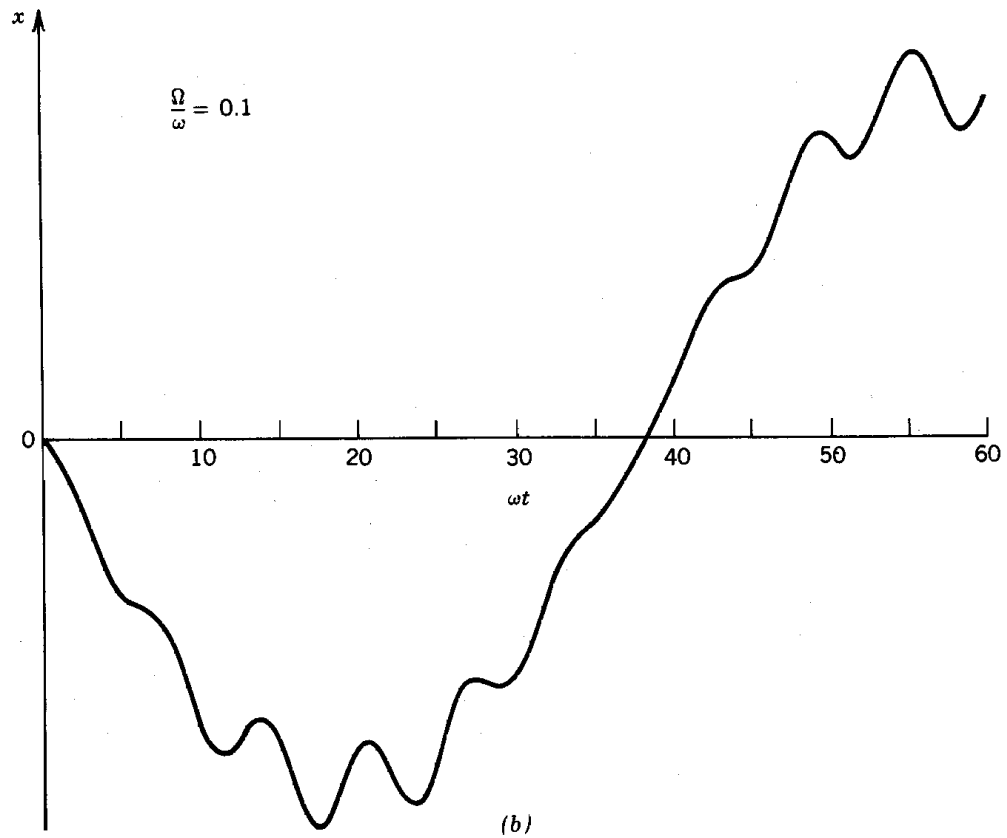


Figure 14.25 (Continued).

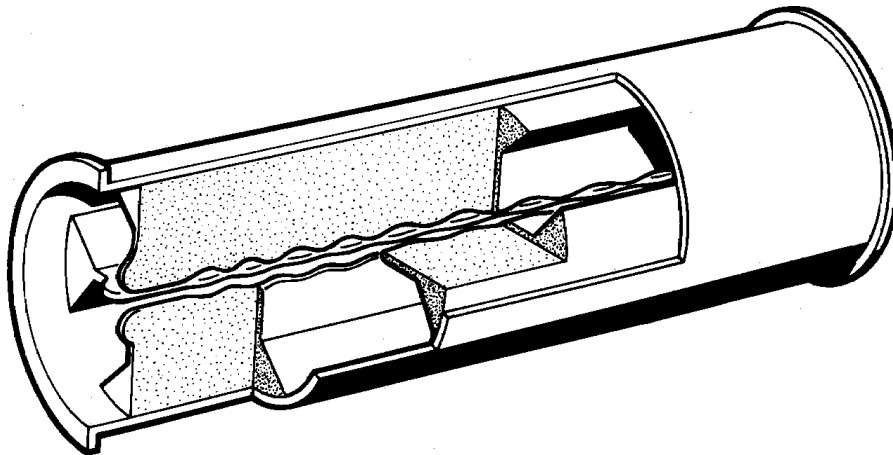


Figure 14.26 General configuration of rf quadrupole. (Courtesy, A. Wadlinger, Los Alamos National Laboratory).

## Radio-frequency Linear Accelerators

The quadrupole lens of Figure 14.24 is useful only for focusing. It exerts no longitudinal force on ions. Axial field components are introduced if the shape of the electrodes is modified to that of Figure 14.26. The distance between the horizontal electrodes and the axis is modulated with spatial period  $D$ . There is a similar modulation of the vertical electrodes  $90^\circ$  out of phase. We postulate transverse fields of the form

$$E_x(x,y,z,t) = (E_o x/a) [1 + \varepsilon \sin(2\pi z/D)] \sin\omega t, \quad (14.93)$$

$$E_y(x,y,z,t) = - (E_o y/a) [1 - \varepsilon \sin(2\pi z/D)] \sin\omega t. \quad (14.94)$$

Again, the electrostatic approximation is invoked near the axis. Following the discussion of Section 4.4, Eqs. (14.93) and (14.94) are valid if (1) they are consistent with the Laplace equation and (2) the generating electrode surfaces lie on an equipotential. We shall show that both conditions can be satisfied.

Assume that a particle enters the system at the origin near time  $t \leq \pi/2\omega$ . The electric fields in the  $x$ - $z$  plane are plotted in Figure 14.27a. The particle experiences a defocusing, quadrupolelike transverse field but also sees an accelerating component of field. Assume further than the particle moves a distance  $D/4$  in the time interval  $\pi/2\omega$ . The particle position and field configuration are sketched at  $t = 3\pi/2\omega$  in Figure 14.27c. Transverse fields are focusing, while the axial component of the electric field is still positive. A synchronous particle orbit can be defined for the system.

We can find the synchronous orbit by determining the axial electric fields and solving the longitudinal equation of motion. If the electrostatic potential field pattern satisfies the Laplace equation, then

$$\partial E_z / \partial z = - (\partial E_x / \partial x + \partial E_y / \partial y). \quad (14.95)$$

Substituting from Eqs. (14.93) and (14.94) and integrating, we find

$$E_z(x,y,z,t) = - (2\varepsilon E_o D / 2\pi a) \cos(2\pi z/D) \sin\omega t. \quad (14.96)$$

The standing wave pattern of Eq. (14.96) can be resolved into two traveling waves,

$$E_z = (\varepsilon E_o D / 2\pi a) [\sin(2\pi z/D + \omega t) - \sin(2\pi z/D - \omega t)]. \quad (14.97)$$

The negative-going wave in the first term can be neglected. The positive-going component will interact strongly with particles moving at the synchronous velocity,

$$v_s = D\omega / 2\pi. \quad (14.98)$$

Assume that the synchronous particle enters the system at the origin of Figure 14.27 with velocity  $v_s$  at time  $t = 0 + \phi/\omega$ . Subsequently, the synchronous particle experiences a constant accelerating axial electric field of magnitude

## Radio-frequency Linear Accelerators

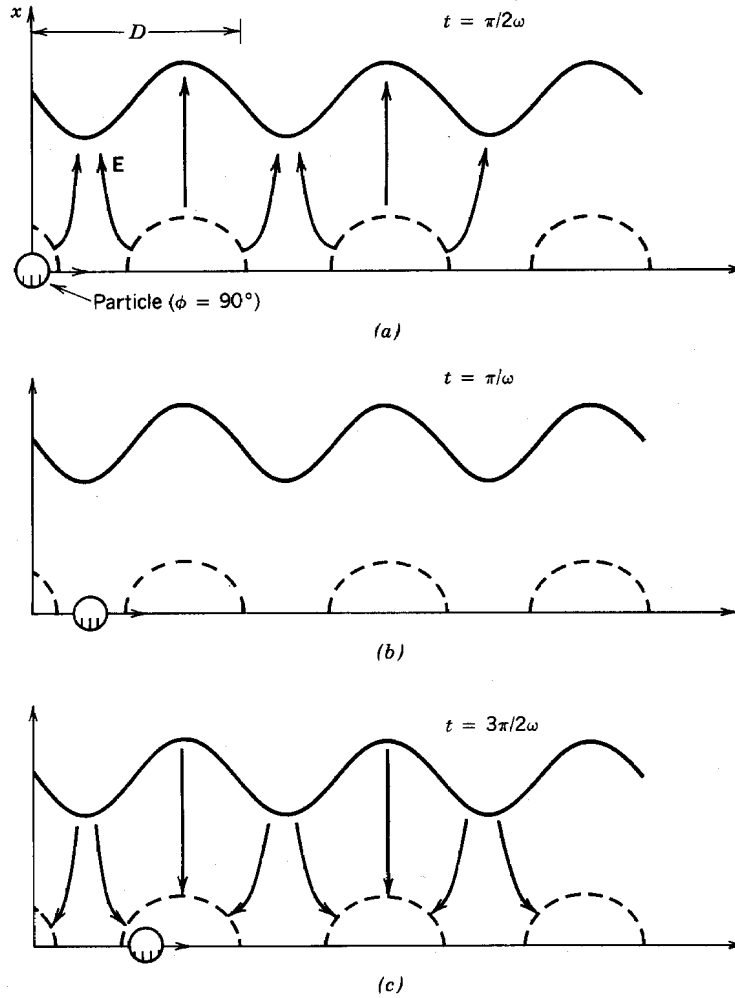


**Figure 14.27** Particle motion and electric fields (projected in  $x$ - $z$  plane) in beam transport region of rf quadrupole. Profile of vertical electrode (vane) designated as solid line; location of horizontal electrode extensions (toward axis) indicated by dashed lines. Particle position corresponds to synchronous particle injected with  $\phi_s = 90^\circ$ ; time measured from zero crossing (positive slope) of vertical vane voltage. (a)  $t = \pi/2\omega$ , particle injected at  $z = 0$ . (b)  $t = \pi\omega$ . (c)  $t = 3\pi/2\omega$ .

$$E_{zs} = (\epsilon E_o D / 2\pi a) \sin\phi. \quad (14.99)$$

The choice of axial origin and rf field phase illustrated in Figure 14.27 makes  $\phi$  synonymous with the particle phase defined in Figure 13.3. As we found in Section 13.1, particle bunches have longitudinal stability if the synchronous phase is in the range  $0 < \phi < 90^\circ$ . In contrast to a drift tube accelerator, an RFQ can be designed with only two traveling wave components. An alternate view is that the RFQ provides almost continuous acceleration. The equation of motion for the synchronous particle is

## Radio-frequency Linear Accelerators

$$m (dv_z/dt) = (\epsilon q E_0 D / 2\pi a) \sin\phi. \quad (14.100)$$

Substituting from Eq. (14.98), Eq. (14.100) can be rewritten as

$$dD/dz = (2\pi\epsilon q E_0 \sin\phi / m\omega^2 a). \quad (14.101)$$

If the field modulation factor  $\epsilon$  is constant, Eq. (14.101) indicates that the length of modulations should increase linearly moving from entrance to exit of the RFQ.

The transverse equation of motion for a particle passing  $z = 0$  at time  $\phi/\omega$  is

$$\begin{aligned} d^2x/dt^2 &= (qE_0 x/ma) [1 + \epsilon \sin(2\pi z/D)] \sin(\omega t + \phi) \\ &= (qE_0 x/ma) \sin(\omega t + \phi) + (\epsilon q E_0 x/2ma) [\cos(2\pi z/D - \omega t - \phi) - \cos(2\pi z/D + \omega t + \phi)]. \end{aligned} \quad (14.102)$$

Again, we retain only the part of the force resonant with synchronous particles. Applying the synchronous condition [Eq. (14.98)], Eq. (14.102) becomes

$$d^2x/dt^2 = (qE_0 x/ma) \sin(\omega t + \phi) + (\epsilon q E_0 x/2ma) \cos\phi. \quad (14.103)$$

The first term on the right-hand side represents the usual transverse focusing from the rf quadrupole. This component of motion is solved by the same method as the axially uniform oscillating quadrupole. The second term represents a defocusing force arising from the axial modulation of the quadrupole electrodes. The origin of this force can be understood by inspection of Figure 14.27. A sequence of particle position and electrode polarities is shown for a particle with a phase near  $90^\circ$ . On the average, the electrode spacing in the  $x$  direction is smaller during transverse defocusing and larger during the focusing phase for  $\phi < 90^\circ$ . This brings about a reduction of the average focusing force.

The solution for average betatron oscillations of particles is

$$x(t) = x_0 \cos\Omega t$$

where

$$\Omega = \sqrt{1/2(qE_0/ma\omega)^2 - (\epsilon q E_0/2ma) \cos\phi}$$

## Radio-frequency Linear Accelerators

The same result is determined for motion in the  $y$  direction. There is net transverse focusing if  $\Omega$  is a real number, or

$$\varepsilon \leq qE_o/(m\omega^2 \cos\phi). \quad (14.105)$$

The longitudinal electric field is proportional to  $\varepsilon$ . Therefore, there are limits on the accelerating gradient that can be achieved while preserving transverse focusing:

$$E_z \leq (qE_o^2 D \tan\phi)/(2\pi a^2 m\omega^2). \quad (14.106)$$

Note that high longitudinal gradient is favored by high pole tip field ( $E_o$ ) and a narrow beam channel ( $a$ ).

The following parameters illustrate the results for the output portion of a 2.5-MeV RFQ operating at 440 MHz. The channel radius is  $a = 0.0025$  m, the synchronous phase is  $\phi = 60^\circ$ , the cell length is 0.05 m, and the pole tip field is 10 MV/m, well below the Kilpatrick limit. The limiting longitudinal gradient is 4.4 MV/m. The corresponding modulation factor is  $\varepsilon = 0.05$ . A typical RFQ design accelerates protons to 2.5 MeV in a length less than 2 m.

Equations (14.93), (14.94), and (14.96) can be used to find the electrostatic potential function following the same method used in Section 4.4. The result is

$$\begin{aligned} \Phi(x,y,z) = & (E_o x^2/2a) [1 + \varepsilon \sin(2\pi z/D)] \\ & - (E_o y^2/2a) [1 - \varepsilon \sin(2\pi z/D)] + (\varepsilon E_o D^2/4\pi^2 a) \sin(2\pi z/D). \end{aligned} \quad (14.107)$$

The equipotential surfaces  $\Phi = \pm E_o a/2$  determine the three-dimensional electrode shape. The equation for the minimum displacement of the vertical vanes from the axis is

$$x_{\min}^2 = [a^2 - (\varepsilon D^2/2\pi^2) \sin(2\pi z/D)]/[1 + \varepsilon \sin(2\pi z/D)].$$

This function is plotted in Figure 14.28. For a modulation factor  $\varepsilon = 0.02$  and an average minimum electrode displacement of 0.0025 m, the distance from the electrode to the axis varies between 0.0019 and 0.0030 m.

The design of RFQ electrodes becomes more complex if the modulation factor is varied to add bunching capability. The design procedure couples results from particle orbit computer codes into a computer-controlled mill to generate complex electrodes such as that illustrated in Figure 14.29. The structure transports an incoming 30-mA, 30-keV proton beam. Electrode modulations increase gradually along the direction of propagation, adding longitudinal field components. The synchronous phase rises from 0 to the final value. Note the increasing modulation depth and cell

## Radio-frequency Linear Accelerators

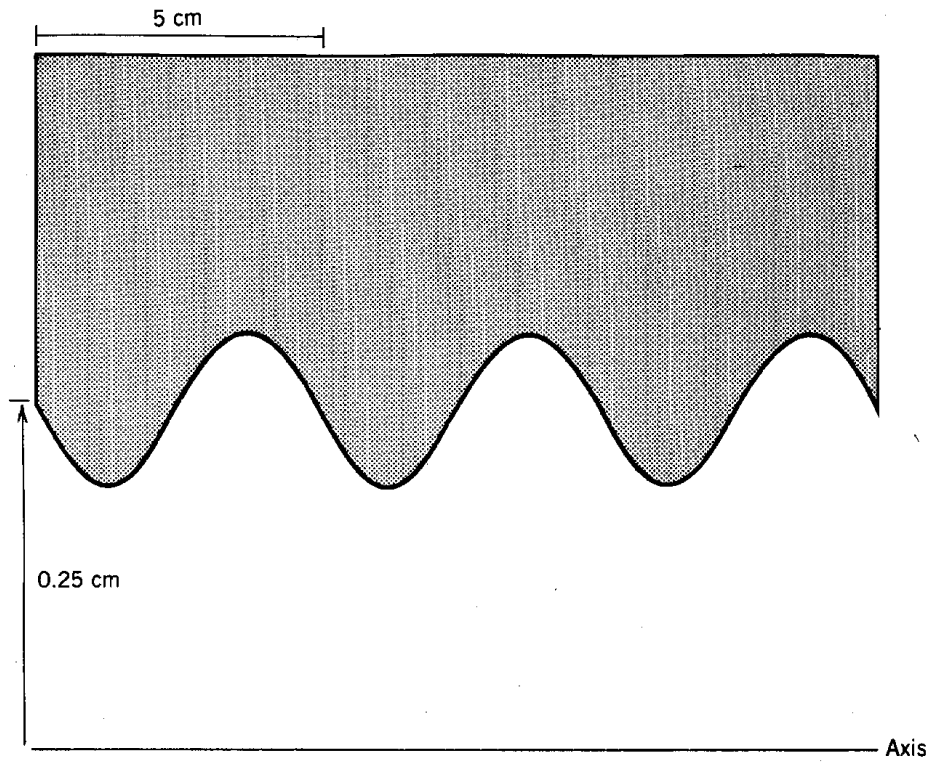


**Figure 14.28** Profile of RFQ electrode. Parameters:  $D = 0.05$  m,  $a = 0.0025$  m,  $\epsilon = 0.02$ .

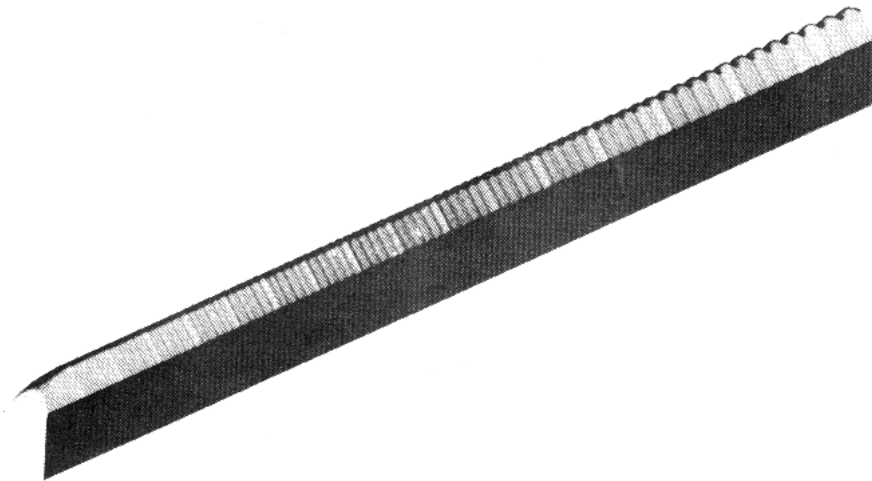
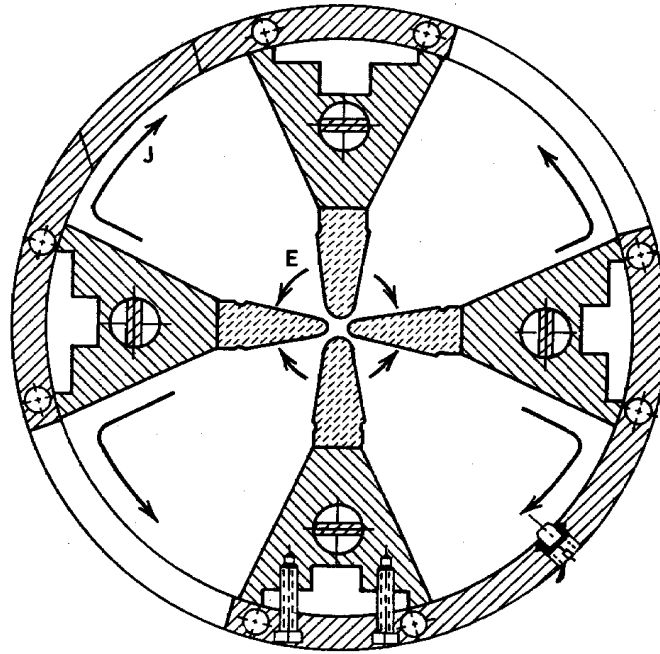
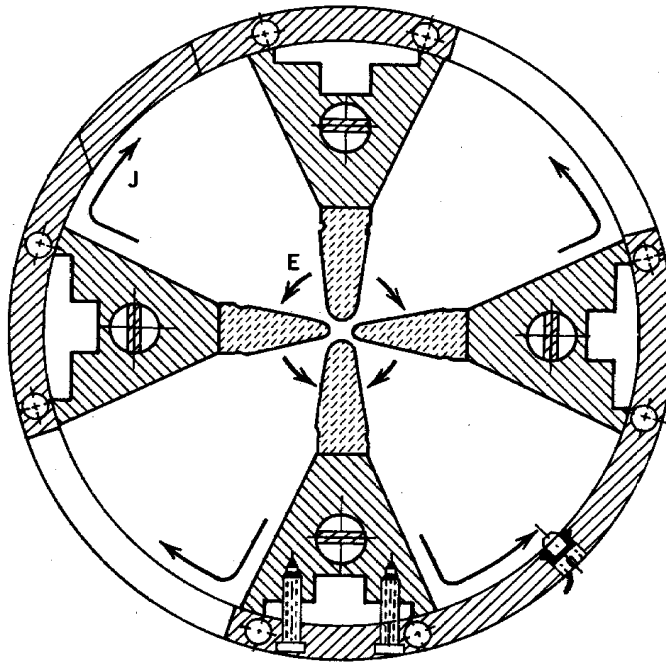


**Figure 14.29** Computer-generated view of RFQ electrode designed for adiabatic bunching and acceleration of low-energy protons. Particles injected at left side. (Courtesy R. Jameson, Los Alamos National Laboratory.)

## Radio-frequency Linear Accelerators



(a)



(b)

**Figure 14.30** Diagram of rf modes in RFQ resonant structure; electric fields and wall currents outside beam transport region. (a) Quadrupole model (b) Dipole mode.

## Radio-frequency Linear Accelerators

length along the direction of acceleration.

A cross section of a complete RFQ is illustrated in Figure 14.30. The volume outside the transport region is composed of four coupled cylindrical section cavities. The desired excitation modes for the cavities have axial magnetic fields and properties which are uniform along the longitudinal direction. Field polarities and current flows are illustrated for the quadrupole mode. A 440-MHz cavity has a radius of about 0.2 m. The mode for the quadrupole oscillation in all four cavities is designated  $TE_{210}$ . This terminology implies the following:

1. Electric fields are transverse to the z direction in the rf portion of the cavity.
2. Field quantities vary in azimuth according to  $\cos(2\theta)$ .
3. The electric field is maximum on axis and decreases monotonically toward the wall.
4. There is no axial variation of field magnitudes in the standing wave.

Coupling of the four lines through the narrow transport region is not strong; equal distribution of energy demands separate drives for each of the lines. The usual procedure is to surround the RFQ with an annular resonator (*manifold*) driven at a single feed point. The manifold symmetrizes the rf energy; it is connected to the transmission lines by multiple coupling slots.

Other modes of oscillation are possible in an RFQ cavity. The dipole mode illustrated in Figure 14.30b is particularly undesirable since it results in electrostatic deflections and beam loss. The dipole mode frequency does not differ greatly from that of the quadrupole. Another practical problem is setting end conditions on the electrodes to maintain a uniform electric field magnitude over the length. Problems of mode coupling and field uniformity multiply as the length of the RFQ increases. This is the main reason why RFQ applications are presently limited to low-energy acceleration. The RFQ has been studied as a pre-accelerator for heavy ions. In this case, the frequency is low. Low-frequency RFQs are sometimes fabricated as a nonresonant structure driven by an oscillator like the Wideröe accelerator.

## 14.7 RACETRACK MICROTRON

The extensive applications of synchrotron radiation to atomic and solid-state physics research has renewed interest in electron accelerators in the GeV range. The microtron is one of the most promising electron accelerators for research. Its outstanding feature is the ability to generate a continuous beam of high-energy electrons with average current approaching 100  $\mu$ A. The time-average output of a microtron is much higher than a synchrotron or high-electron linac, which produce pulses of electrons at relatively low repetition rates.

The racetrack microtron [V.Veksler, *Compt. Rend. Acad. Sci. U. S. S. R.* **43**, 444 (1944)] is illustrated in Figure 14.31a. Electrons are accelerated in a short linac section. Uniform field sector

## Radio-frequency Linear Accelerators

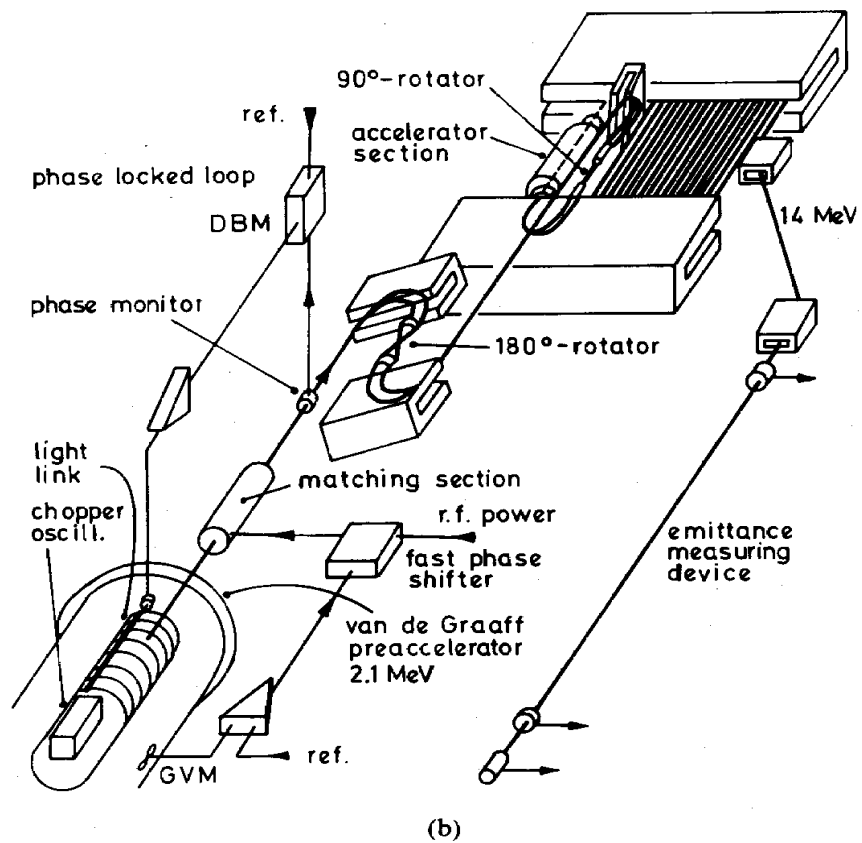
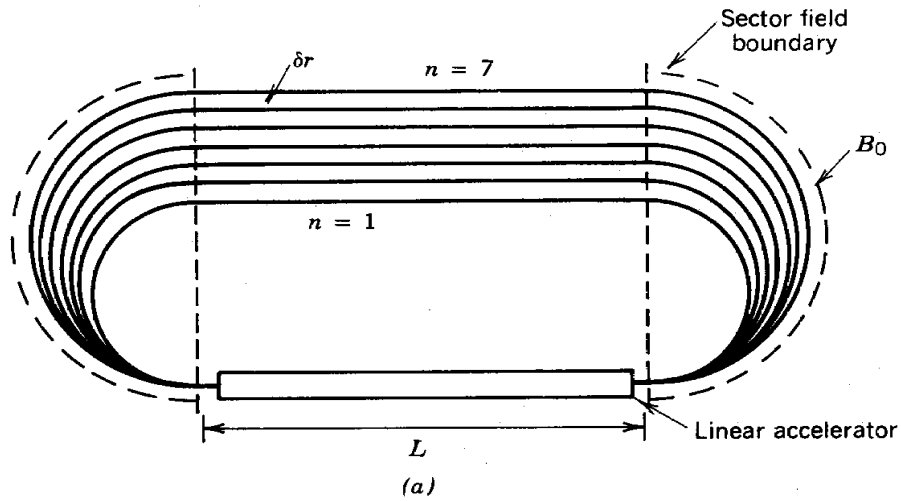


**Figure 14.31** Racetrack microtron. (a) Section view of components and electron orbits after from one to seven passes through linear accelerator. (b) Isometric view of microtron components and injection system for MAMI I. (Courtesy H. Herminghaus, Universität Mainz.)

## Radio-frequency Linear Accelerators

magnets at each end of the accelerator confine the electrons. Electrons at a variety of energy levels are contained simultaneously in the machine. Electron orbits in the magnets are half-circles. It is easily demonstrated that electrons return to the linear accelerator axis after each revolution, independent of their energy. The size of the orbit increases as the electron energy increases.

The microtron combines linear accelerator technology with circular accelerator particle dynamics. Beam recirculation allows more efficient utilization of the linac. In contrast to the high-energy electron linear accelerators of Section 14.1 (where the machine length is a major constraint), acceleration gradient is not the primary concern in the microtron. This means that the accelerator need not operate at high field stress; therefore, power dissipation is a factor of 25-100 times lower than a high-gradient electron linac. This accounts for the capability of CW steady-state operation. The phase velocity of traveling wave components in the microtron linac is equal to the speed of light. In contrast to high-energy electron linacs, microtrons have phase stability. The orbit size (and, hence, the time to return to the linac) depends on electron energy. Therefore, electrons can be longitudinally confined during acceleration, even at low values of accelerating gradient.

Some parameters of a medium-energy microtron are listed in Table 14.5. The machine is designed as a pre-accelerator in a three-microtron facility to produce an 840-MeV beam. The 14-MeV microtron with its associated injection and extraction system is illustrated in Figure 14.31b. The injected beam is generated by a 2-MV Van de Graaff accelerator. A beam chopper in the terminal of the electrostatic accelerator produces short pulses of electrons phased-matched to the linac. The complex series of lenses and deflection magnets matches the transverse and longitudinal distributions of the electron beam to the acceptance of the microtron. The origin of the parameters in Table 14.5 will be evident after we develop the theory of microtron equilibrium orbits.

In order to describe the microtron analytically, assume that the sector fields have sharp boundaries and a uniform field magnitude,  $B_0$ . Electrons are injected with initial total energy  $U_0$  and gain an energy  $\Delta U$  in each pass through the linear accelerator. Assume, further, that  $U_0 \gg m_e c^2$ , so that the electron velocity is always approximately equal to the speed of light. We have shown that acceleration in linear accelerators arises from a traveling wave component of the form

$$E_z = E_0 \sin(\omega t - \omega z/c).$$

The energy gain of a relativistic electron traversing an accelerator of length  $L$  is

$$\Delta U = eE_0 L \sin\phi,$$

where  $\phi$  is the phase of the particle with respect to the traveling wave. The energy gain for synchronous electrons passing through the linac is independent of their total energy.

The index  $n$  designates the number of times that an electron has passed through the linear accelerator; the orbits in Figure 14.31 are labeled accordingly. The time for an electron to traverse the microtron is

$$\Delta t_n = 2L/c + 2\pi r_{gn}/c, \quad (14.108)$$

## Radio-frequency Linear Accelerators

**TABLE 14.5 Parameters of MAMI, Stages I and II<sup>a</sup>**

	Stage I	Stage II
<i>General</i>		
Input energy	2.1 MeV	14 MeV
Output energy	14 MeV	175 MeV
Number of traversals	20	51
Power consumption (total)	280 kW	
Design current	100 $\mu$ A	
<i>Magnet System</i>		
Magnet separation	1.66 m	5.59 m
Magnetic field	0.10 T	0.54 T
Maximum orbit diameter	0.97 m	2.17 m
Magnet weight (each)	1.3 tonne	43 tonne
Gap width	6 cm	7 cm
<i>rf System</i>		
Linac length	0.80 m	3.55 m
Numbers of klystrons	2	
Frequency	2.449 GHz	
rf power	9 kW	64 kW
Beam load	1.2 kW	16 kW
Energy gain per turn	0.59 MeV	3.16 MeV

<sup>a</sup>Nuclear Physics Institute, University of Mainz.

where

$$r_{gn} = \gamma_n m_e c / eB_o = U_n / eB_o c.$$

The quantity U is the total energy of an electron on the  $n$ th orbit:

$$U_n = U_o + n\Delta U. \quad (14.109)$$

The condition for synchronous electrons is that they arrive at the entrance to the linac at the same phase of the rf period. In other words, the traversal time must be an integer multiple of the rf period. Letting  $\omega$  be the frequency of rf oscillations in the linac, this condition is written

$$\Delta t_n = 2L/c + 2\pi U_n / eB_o c^2 = m(2\pi/\omega). \quad (14.110)$$

## Radio-frequency Linear Accelerators

As electrons gain energy, the particle velocity is constant but the orbit size increases. The traversal time of high-energy particles is longer than that of low-energy particles. The difference in traversal times between particles on the  $n$  and  $n-1$  orbits is

$$\Delta t_n - \Delta t_{n-1} = 2\pi\Delta U/eB_o c^2. \quad (14.111)$$

Clearly, for synchronization  $\Delta t_n$  must also equal an integer multiple of the rf period:

$$2\pi\Delta U/eB_o c^2 = q (2\pi/\omega). \quad (14.112)$$

As an example, we pick  $q = 1$ . This means that electrons take one extra rf period for a traversal with each energy increment. Following Table 14.5, assume a 20-turn microtron with an injection energy of 2 MeV. The bending magnetic field is 0.1 T, and the linear accelerator length is 0.8 M. The energy gain per turn is  $\Delta U = 0.6$  MeV, implying an average acceleration gradient of 0.75 MV/m. Substituting into Eq. (14.112), the matched frequency is  $\omega = 1.5 \times 10^{10} \text{ s}^{-1}$ , or  $f = 2.4$  GHz. Electrons injected at 2 MeV are boosted to 2.6 MeV in their first passage through the linac. The initial gyroradius in the bending field is 0.174 m; the total distance around the system on the first orbit is 2.7 m. Equation 14.111 implies that the time for the first traversal equals 22 rf periods. This is a high number; the particle must return to the linac entrance with equal phase after an interval of  $22(2\pi/\omega)$ . Synchronization requires excellent bending field uniformity and a constant energy input beam with little velocity dispersion. The problem becomes more acute as electrons are accelerated. Electrons on the highest-energy orbit take 42 rf periods to traverse the system. The synchronization problem limits the practical number of turns in a single microtron. A choice of  $q > 1$  worsens the problem.

The separation between adjacent orbits on the side opposite the linac is

$$\delta r \cong 2\Delta r_g \cong \Delta U/eB_o c.$$

For the parameters of the example,  $\delta r = 0.04$  in. The large orbit separation makes extraction of high-energy electrons relatively easy.

The two main problems of microtrons are beam steering and beam breakup instabilities. Regarding the first problem, the uniform magnetic field of the microtron has horizontal focusing but no vertical focusing. Lenses must be added to each beam line on the straight sections opposite the accelerator. Even with the best efforts to achieve bending field uniformity, it is necessary to add beam steering magnets with active beam sensing and compensation to meet the synchronization condition. The beam breakup instability is severe in the microtron because the current of all beams is concentrated in the high-Q resonant cavities of the linear accelerator. The beam breakup instability is the main reason why microtron average currents are limited to less than 1 mA. It has also impeded the development of microtrons with superconducting linear accelerator cavities. These cavities have extremely high values of Q for all modes.

## Radio-frequency Linear Accelerators

Phase stability is an interesting feature of microtrons. In contrast to high-energy electron linear accelerators, variations of electron energy lead to phase shifts because of the change in orbit pathlength. For instance, a particle with energy greater than that of the synchronous particle has a larger gyroradius; therefore, it enters the linac with increased phase. For longitudinal stability, the higher-energy electrons must receive a reduced energy increment in the linac. This is true if the synchronous phase is in a region of decreasing field,  $90^\circ \leq \phi_s \leq 180^\circ$ . Particle phase orbits are the inverse of those in a linear ion accelerator.

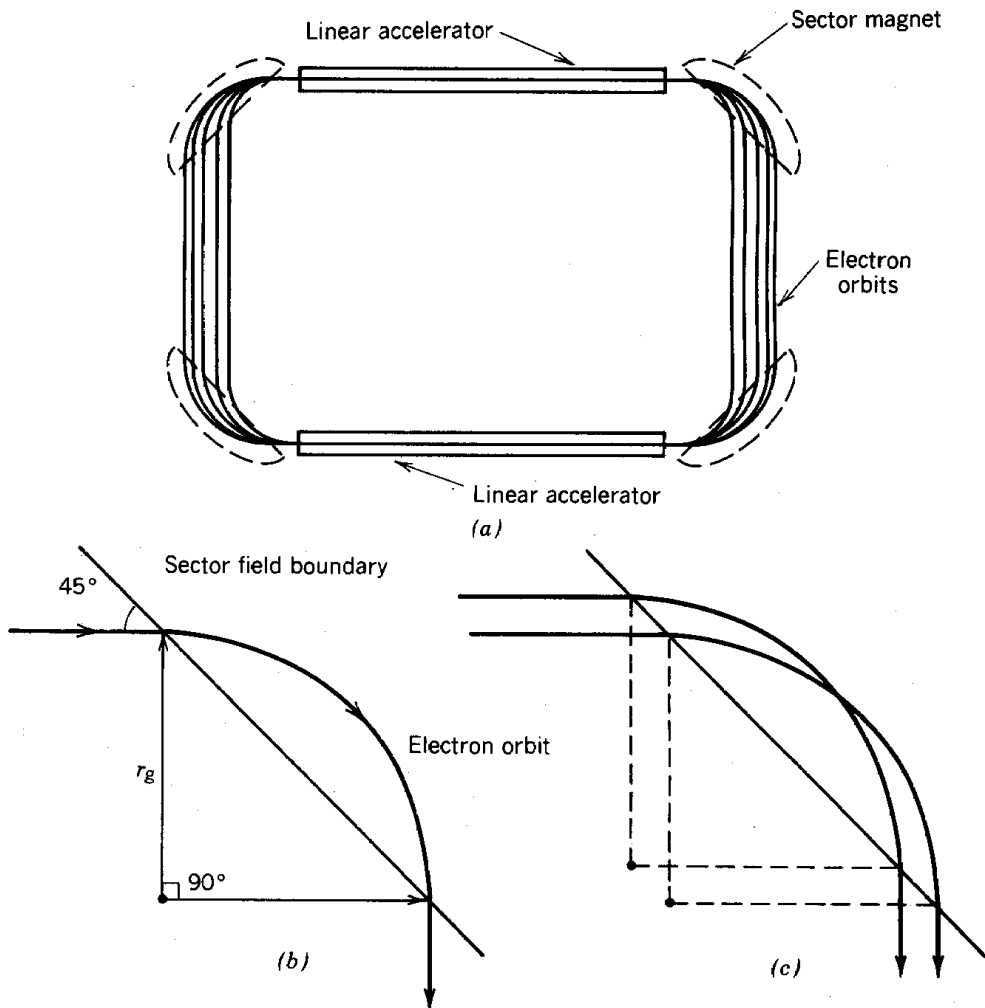


**Figure 14.32** Double-sided microtron. (a) Sectional view of components and particle orbits. (b) Specular reflection of particle orbit incident on  $45^\circ$  sector magnet. (c) Neutral focusing property of  $45^\circ$  sector magnet.

## Radio-frequency Linear Accelerators

The double-sided microtron (DSM) illustrated in Figure 14.32a is an alternative to the racetrack microtron. The DSM has linear accelerators in both straight sections. Beam deflection is performed by four  $45^\circ$  sector magnets. The major advantage, compared to the racetrack microtron, is that approximately double the electron energy can be achieved for the same magnet mass. The  $45^\circ$  sector magnet has the feature that the orbits of electrons of any energy are reflected at exactly  $90^\circ$  (see Fig. 14.32b).

Unfortunately, the DSM has unfavorable properties for electron focusing. Figure 14.32c shows a particle trajectory on the main orbit compared to an orbit displaced horizontally off-axis. Note that there is no focusing; the DSM has neutral stability in the horizontal direction. Furthermore, the sector magnets contribute defocusing forces in the vertical direction. There are edge-focusing effects because the magnets boundaries are inclined  $45^\circ$  to the particle orbits. Reference to Section 6.9, shows that the inclination gives a negative focal length resulting in defocusing.